American Mineralogist, Volume 101, pages 1389–1405, 2016

High concentrations of manganese and sulfur in deposits on Murray Ridge, Endeavour Crater, Mars

Raymond E. Arvidson[1,*], Steven W. Squyres[2], Richard V. Morris[3], Andrew H. Knoll[4], Ralf Gellert[5], Benton C. Clark[6], Jeffrey G. Catalano[1], Brad L. Jolliff[1], Scott M. McLennan[7], Kenneth E. Herkenhoff[8], Scott VanBommel[5], David W. Mittlefehldt[3], John P. Grotzinger[9], Edward A. Guinness[1], Jeffrey R. Johnson[10], James F. Bell III[11], William H. Farrand[6], Nathan Stein[1], Valerie K. Fox[1], Matthew P. Golombek[12], Margaret A.G. Hinkle[1], Wendy M. Calvin[13], and Paulo A. de Souza Jr.[14]

[1]Department of Earth and Planetary Sciences, Washington University in Saint Louis, St. Louis, Missouri 63130, U.S.A.
[2]Department of Astronomy, Cornell University, Ithaca, New York 14853, U.S.A.
[3]Johnson Space Center, Houston, Texas 77058, U.S.A.
[4]Department of Organismic and Evolutionary Biology, Harvard University, Cambridge, Massachusetts 02138, U.S.A.
[5]Department of Physics, University of Guelph, Guelph, Ontario N1G 2W1, Canada
[6]Space Science Institute, Boulder, Colorado 80301, U.S.A.
[7]Department of Geosciences, Stony Brook University, Stony Brook, New York 11794, U.S.A.
[8]U.S. Geological Survey, Astrogeology Science Center, Flagstaff, Arizona 86001, U.S.A.
[9]Division of Geological and Planetary Sciences, California Institute of Technology, Pasadena, California 91125, U.S.A.
[10]Johns Hopkins University, Applied Physics Laboratory, Laurel, Maryland 20723, U.S.A.
[11]School of Earth & Space Exploration, Arizona State University, Tempe, Arizona 85281, U.S.A.
[12]California Institute of Technology/Jet Propulsion Laboratory, Pasadena, California 91011
[13]Geological Sciences and Engineering, University of Nevada, Reno, Nevada 89503, U.S.A.
[14]CSIRO Digital Productivity Flagship, Hobart, Tasmania 7004, Australia

Abstract

Mars Reconnaissance Orbiter HiRISE images and Opportunity rover observations of the ~22 km wide Noachian age Endeavour Crater on Mars show that the rim and surrounding terrains were densely fractured during the impact crater-forming event. Fractures have also propagated upward into the overlying Burns formation sandstones. Opportunity's observations show that the western crater rim segment, called Murray Ridge, is composed of impact breccias with basaltic compositions, as well as occasional fracture-filling calcium sulfate veins. Cook Haven, a gentle depression on Murray Ridge, and the site where Opportunity spent its sixth winter, exposes highly fractured, recessive outcrops that have relatively high concentrations of S and Cl, consistent with modest aqueous alteration. Opportunity's rover wheels serendipitously excavated and overturned several small rocks from a Cook Haven fracture zone. Extensive measurement campaigns were conducted on two of them: Pinnacle Island and Stuart Island. These rocks have the highest concentrations of Mn and S measured to date by Opportunity and occur as a relatively bright sulfate-rich coating on basaltic rock, capped by a thin deposit of one or more dark Mn oxide phases intermixed with sulfate minerals. We infer from these unique Pinnacle Island and Stuart Island rock measurements that subsurface precipitation of sulfate-dominated coatings was followed by an interval of partial dissolution and reaction with one or more strong oxidants (e.g., O_2) to produce the Mn oxide mineral(s) intermixed with sulfate-rich salt coatings. In contrast to arid regions on Earth, where Mn oxides are widely incorporated into coatings on surface rocks, our results demonstrate that on Mars the most likely place to deposit and preserve Mn oxides was in fracture zones where migrating fluids intersected surface oxidants, forming precipitates shielded from subsequent physical erosion.

Keywords: Mars, geochemistry, mineralogy, manganese oxides, sulfates

Introduction

Recent observations by the Opportunity Mars rover on the Cape York rim segment of the Noachian-age 22 km wide Endeavour Crater (Fig. 1) revealed evidence for aqueous mobilization of Zn and precipitation of gypsum in veins (Squyres et al. 2012), together with the formation of phyllosilicate minerals in and along fractures (Arvidson et al. 2014). In parallel, the Curiosity rover in Gale Crater has uncovered morphologic, compositional, and mineralogic evidence for a broadly coeval fluvial-deltaic-lacustrine system and associated diagenetic alteration of sedimentary rocks of basaltic composition (Grotzinger et al. 2014, 2015). These discoveries add to the growing evidence from

* E-mail: arvidson@wunder.wustl.edu
Open access: Article available to all readers online.

0003-004X/16/0006–1389$05.00/DOI: http://dx.doi.org/10.2138/am-2016-5599

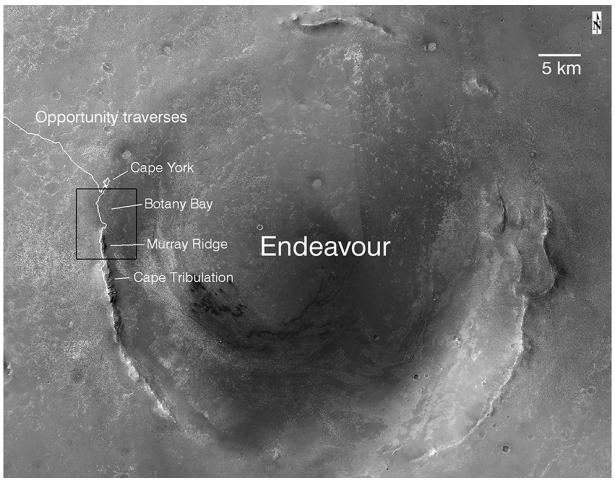

Figure 1. HiRISE-based mosaic showing Endeavour Crater, Opportunity's traverses, and key locations on the crater rim explored by the rover. Endeavour is largely buried by later Burns formation sulfate-rich sandstones and thus only high portions of the crater rim are exposed. Box shows the location of the portion of the mosaic shown in Figure 2.

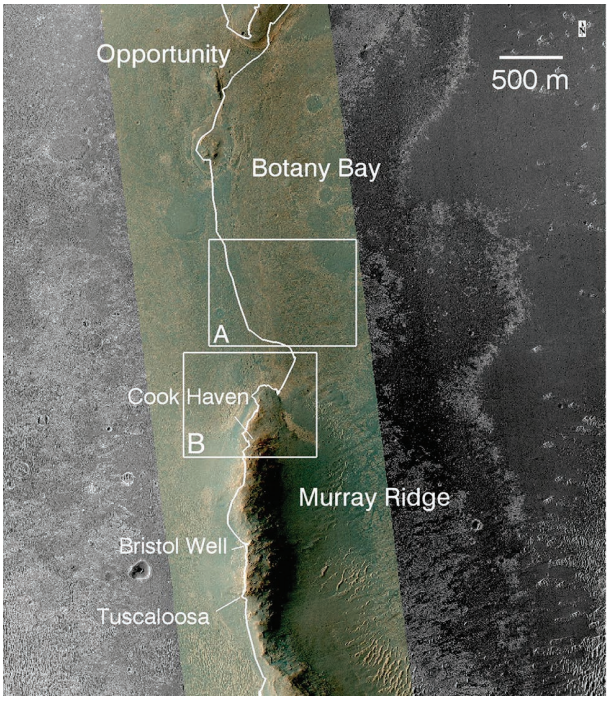

Figure 2. HiRISE-based image showing Botany Bay and Murray Ridge, with Opportunity's traverses shown. Cook Haven is a gentle swale on the Murray Ridge rim segment and was the site for Opportunity's sixth winter sojourn. Bristol Well is a Ca sulfate vein and Tuscaloosa is a breccia outcrop examined by Opportunity, and both are shown to provide context for the rover's exploration of Murray Ridge. Box A is the location shown in Figure 3 that illustrates concentric and radial fractures in the Burns formation. Box B is the location shown in Figure 4 that shows fractures and the northern portion of Murray Ridge. HiRISE image ESP_036753_1775_MRGB (merged color and grayscale).

orbital and landed missions that early Mars supported extensive water-related alteration of crustal materials in both surface and subsurface environments (e.g., Poulet et al. 2005; Ehlmann and Edwards 2014). In this paper we describe measurements acquired by Opportunity while exploring the Murray Ridge rim segment of Endeavour Crater (Figs. 2–4, Table 1). We first provide an overview of Opportunity's traverses and measurements on Murray Ridge and consider the implications for past aqueous processes based on exposed bedrock measurements. We then focus on rocks named Pinnacle Island and Stuart Island that were serendipitously excavated from a fracture by Opportunity's wheels. These rocks have unique coatings with the highest Mn and S concentrations found thus far at Meridiani Planum. The data imply aqueous precipitation of sulfate-rich salts, followed by introduction of a strong oxidant that led to precipitation of one or more Mn oxide(s).

Opportunity Rover and Instrument Payload

Opportunity is a six-wheeled, solar-powered rover (Squyres et al. 2003) equipped with mast-based Pancam multispectral stereo cameras with 13 filters covering the 0.432 to 1.009 μm spectral region (Bell et al. 2003), a robotic arm (instrument deployment device or IDD) with a microscopic imager (MI) that can acquire panchromatic images with 31 μm pixel sizes (Herkenhoff et al. 2003), an alpha particle X-ray spectrometer (APXS) to determine the target chemical compositions (Gellert et al. 2006), and a rock abrasion tool (RAT) to brush loose dust and sand from targets and/or to grind into rocks to remove indurated coatings or weathering rinds (Gorevan et al. 2003). In addition, the rover carries mast-mounted stereo cameras for navigation and terrain context measurements (Navcams), and front and rear body-mounted stereo cameras (Hazcams) used for hazard avoidance during traverses and fine-scale placement of IDD-based instruments onto rock and soil targets. The science instrument payload also includes the Mini-TES thermal emission spectrometer and a Mössbauer spectrometer, but these two instruments were no longer functioning during the time period covered by this paper.

Structural Geology of Endeavour Crater

Endeavour is a complex impact crater that is largely buried by younger sulfate-rich sandstones of the Burns formation (Squyres et al. 2012; Crumpler et al. 2015; Grant et al. 2015). The exposed rim is divided into discrete segments separated by relatively low regions covered by Burns formation rocks. The presence of extensive breccia outcrops of the Shoemaker formation on Cape York and Murray Ridge confirms that the crater formed by a bolide impact (Squyres et al. 2012; Arvidson et al. 2014; Crumpler et al. 2015). Comparison to martian impact craters of similar size indicates that only ~100 to 200 m of rim material has been removed by erosion, mostly by fluvial activity before deposition of Burns formation materials (Grant et al. 2015). Thus, exploration and characterization of Endeavour's rim by Opportunity provide detailed ground truth information about the lithologic nature and extent of alteration by aqueous fluids for the rim of a Noachian-age complex impact crater.

Structural observations of complex terrestrial impact craters similar in size to Endeavour provide insight into the types of

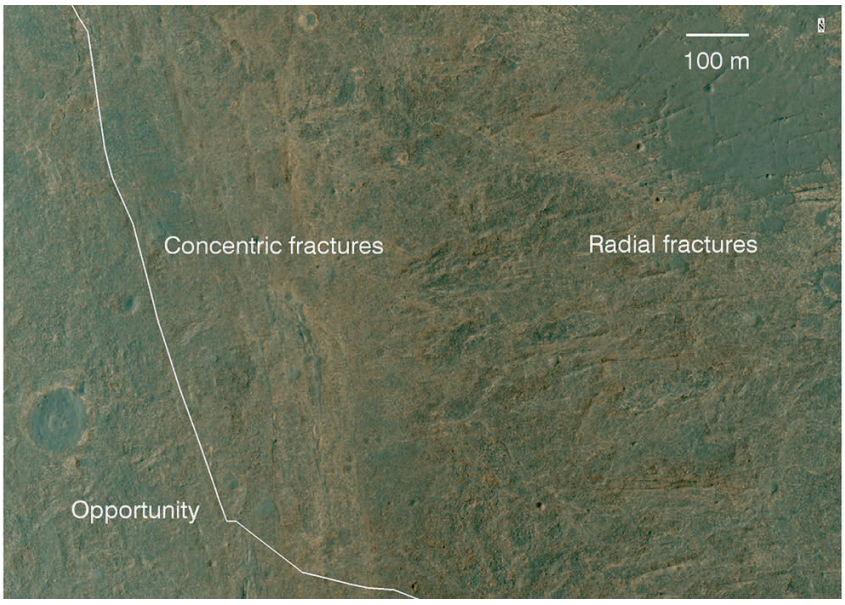

FIGURE 3. Portion of the HiRISE-based image segment covering Botany Bay, highlighting the locations of concentric fractures that are interpreted to have propagated up through the Burns formation outcrops just above a buried portion of Endeavour's rim between the Cape York and Murray Ridge rim segments. Radial fractures are evident extending to the east and northeast into Endeavour. HiRISE image ESP_036753_1775_MRGB.

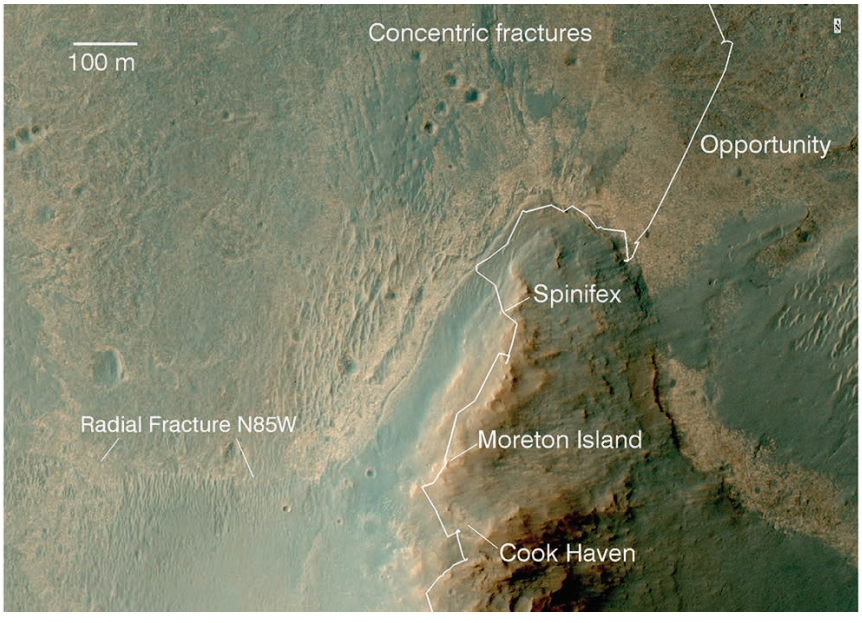

FIGURE 4. Portion of the HiRISE-based image segment covering the northern part of Murray Ridge. Concentric fractures are evident extending into the Burns formation outcrops located to the north of Murray Ridge. Note the radial fracture (strike N85°W) extending from the west to the east, terminating near the Cook Haven location. Spinifex and Moreton Island are two of Opportunity's breccia outcrop targets and are shown for context. HiRISE image ESP_036753_1775_MRGB.

fractures expected on the rim segments and surrounding terrains explored by Opportunity. In particular, the Ries Crater, which is ~26 km in diameter (Stöffler et al. 2013), the ~23 km diameter Haughton Crater (Osinski and Spray 2005), and the ~22 km wide Gosses Bluff impact structure (Milton et al. 1972) have been studied in detail and exhibit extensive fractures that formed both radially and concentrically to the crater centers. Osinski and Spray (2005) and Kenkmann et al. (2014) provide schematic views of structural patterns generated during the collapse stage of complex crater formation. Their models, supported by

TABLE 1. APXS compositional data for the western portion of Murray Ridge, including Cook Haven localities for key measurements discussed in this paper

Sol	3463	3498	3502	3522	3535	3542	3546	3548	3551	3560	3564
Type[a]	RB	RU	RU	RU	RU	RB	RU	RU	RU	RU	RU
Target	Spinifex	Tanga-looma	Mount Tempest	Cape Darby	Cape Darby 2	Cape Elizabeth	Pinnacle Island	Pinnacle Island 2	Pinnacle Island 3	Pinnacle Island 4	Pinnacle Island 5
Norm	76	68	72	66	73	74	31	39	41	28	40
SiO_2	45.7	45.7	46.3	46.3	45.5	44.7	28.1	23.8	18.1	36.2	20.1
TiO_2	1.04	1.09	1.16	1.13	1.18	0.96	0.76	0.62	0.44	0.91	0.58
Al_2O_3	8.76	9.43	10.30	9.39	9.23	9.06	5.75	4.70	3.48	7.57	3.68
Cr_2O_3	0.22	0.20	0.21	0.25	0.27	0.20	0.21	0.12	0.10	0.22	0.10
FeO_T[b]	17.6	16.2	16.1	17.0	17.1	16.7	16.6	16.0	15.1	17.9	15.5
MnO_T[b]	0.78	0.36	0.40	0.31	0.35	0.26	1.67	2.12	3.48	1.30	3.35
MgO	8.85	8.58	7.48	6.96	7.13	8.01	12.06	13.26	13.00	9.43	11.50
CaO	6.18	6.29	7.14	6.67	6.47	5.92	5.45	6.08	7.66	5.69	8.26
Na_2O	2.32	2.04	2.39	2.25	2.37	2.54	1.01	1.02	0.86	1.57	0.84
K_2O	0.70	0.23	0.30	0.46	0.49	0.36	0.32	0.17	0.14	0.41	0.13
P_2O_5	1.18	1.15	1.18	0.97	0.98	0.89	1.57	2.18	2.37	1.33	2.44
SO_3	5.52	7.82	6.25	7.20	7.66	9.17	25.44	28.81	34.51	16.44	32.70
Cl	0.95	0.74	0.75	1.06	1.17	1.12	0.92	0.95	0.66	0.91	0.65
Ni (ppm)	537	523	342	394	394	447	661	884	1001	354	736
Zn (ppm)	460	118	87	258	203	121	185	130	155	204	116
Br (ppm)	706	97	43	112	110	78	262	476	334	144	269

Sol	3569	3573	3574	3575	3577	3581	3583	3587	3598	3664	3666
Type[a]	RB	RU	RU	RU	RU	SD	SD	RU	RB	RU	RU
Target	Green Island	Stuart Island 1	Stuart Island 2	Stuart Island 3	Stuart Island 4	Anchor Point 1	Anchor Point 2	Sledge Island 1	Turnagain Arm	Bristol Well 1	Bristol Well 2
Norm	78	75	82	65	73	59	78	63	76	66	66
SiO_2	43.3	27.3	22.5	16.1	25.6	37.8	39.3	47.6	44.5	42.8	41.9
TiO_2	1.02	0.78	0.65	0.57	0.65	0.95	1.07	0.63	1.04	0.94	0.92
Al_2O_3	8.89	5.67	4.38	3.60	4.87	7.00	7.86	10.44	9.10	8.50	8.25
Cr_2O_3	0.19	0.13	0.17	0.14	0.16	0.35	0.38	0.21	0.20	0.27	0.26
FeO_T[b]	16.7	16.2	16.5	17.0	16.8	18.2	18.3	12.8	16.4	15.1	14.8
MnO_T[b]	0.27	1.57	2.01	2.85	3.37	0.75	1.01	0.30	0.28	0.34	0.33
MgO	7.31	12.31	14.49	15.58	11.65	8.14	8.52	6.35	8.05	6.98	6.86
CaO	6.38	5.36	3.75	4.05	4.85	7.28	7.07	9.65	5.98	9.42	10.00
Na_2O	2.53	0.93	0.82	0.53	0.86	1.74	1.92	2.48	2.32	2.15	2.03
K_2O	0.37	0.18	0.12	0.09	0.28	0.33	0.35	0.28	0.36	0.49	0.45
P_2O_5	0.99	1.08	0.91	0.98	1.40	1.82	1.53	0.82	0.95	1.01	1.06
SO_3	10.48	28.20	33.31	38.21	28.95	15.09	12.06	7.74	9.37	11.00	12.04
Cl	1.54	0.22	0.26	0.21	0.33	0.43	0.45	0.65	1.36	0.95	0.97
Ni (ppm)	376	547	715	1024	1022	372	603	123	453	312	269
Zn (ppm)	152	82	111	175	231	218	198	138	114	321	302
Br (ppm)	65	40	88	77	77	117	180	94	167	75	81

Sol	3667	3671	3675	3676	3707	3708	3709		
Type[a]	RU	RB	RU	RU	RU	RU	RU	Avg. stat. error (%)	Approx. accuracy (%)
Target	Bristol Well 3	Sarcobatus Flat 1	Sarcobatus Clast	Sarcobatus Clast 2	Sodaville	Tusca-loosa	Sodaville 2		
Norm	50	76	37	41	65	73	47		
SiO_2	45.4	44.9	46.0	46.2	45.4	45.9	45.6	2	4
TiO_2	1.15	0.98	1.15	1.41	1.11	1.05	1.12	10	20
Al_2O_3	8.89	8.84	9.89	11.23	9.18	9.10	9.25	2	7
Cr_2O_3	0.27	0.23	0.20	0.14	0.28	0.19	0.24	25	20
FeO_T[b]	17.6	17.6	16.5	15.3	18.0	17.1	17.7	2	10
MnO_T[b]	0.36	0.24	0.51	0.27	0.25	0.14	0.23	10	10
MgO	7.14	7.78	6.98	6.21	7.42	8.20	7.34	3	15
CaO	7.17	6.38	7.72	8.17	6.56	6.20	6.75	2	7
Na_2O	2.03	2.30	1.90	2.00	2.29	2.13	2.22	15	15
K_2O	0.50	0.48	0.51	0.44	0.55	0.41	0.52	10	15
P_2O_5	1.00	1.17	1.09	1.61	1.01	1.11	1.07	10	15
SO_3	7.36	7.10	6.40	6.12	6.69	7.18	6.56	2	15
Cl	1.05	1.92	1.06	0.83	1.12	1.19	1.24	4	30
Ni (ppm)	365	293	193	292	391	371	305	15	15
Zn (ppm)	361	162	295	151	372	132	325	10	15
Br (ppm)	102	98	69	69	71	117	87	10	20

Notes: Values are oxide concentrations unless otherwise indicated. Also given in the table are the average percentage uncertainty for each element representing the statistical error for each measured spot (Gellert et al. 2006). These are typically better for higher abundances and worse for lower. The last column gives the average relative accuracy for each element found for the MER APXS calibration with homogeneous powdered geological reference samples (Gellert et al. 2006).

[a] Abbreviations for Type: RU = rock, unbrushed; RB = rock, brushed; SD = soil, disturbed.

[b] Total Fe reported as FeO (FeO_T) and Mn as MnO_T.

observations, imply that concentric and radial fractures should cut through rim structures of complex craters. These fractures should also propagate upward through deposits generated after the impact event by reactivation during later local- to regional-scale tectonic activity and/or increased stresses associated with loading as later deposits accumulate.

Mars Reconnaissance Orbiter HiRISE images offer 0.25 m/pixel ground resolution, with an imaging system modulation transfer function that preserves fine spatial details of the martian surface (McEwen et al. 2007). Examination of HiRISE images

for Endeavour rim and inter-rim segments traversed by Opportunity show evidence for both concentric and radial fractures, including systems that have propagated upward into Burns formation materials. For example, the Burns formation bedrock in Botany Bay hosts fractures that are approximately parallel or perpendicular to the rim segments (Fig. 3). In addition, several fractures are evident extending westward from Murray Ridge into the surrounding Burns formation materials (Fig. 4). As will be shown in the next section of this paper, Opportunity-based images demonstrate that the impact breccia outcrops on Murray Ridge exhibit extensive fracturing that is consistent with the formation of Endeavour Crater and later readjustments.

Opportunity's exploration of Murray Ridge

Opportunity traversed from outcrops of Burns formation sandstones onto the Shoemaker and underlying Matijevic formation rocks (Squyres et al. 2012; Arvidson et al. 2014; Crumpler et al. 2015) exposed on the Cape York rim segment of Endeavour Crater in 2011. The rover explored this rim segment until it was commanded to head south and enter Botany Bay. Opportunity then crossed the Burns formation outcrops in Botany Bay and approached its first outcrop on the northeastern corner of Murray Ridge (Fig. 1). After conducting several measurements on this portion of the rim, Opportunity was commanded to drive around the northern nose of Murray Ridge (Solander Point) and begin a thorough exploration and characterization of its western slopes. The western side of Murray Ridge was chosen because of extensive outcrops and less steep terrain than the interior portion of the Ridge. Opportunity is a solar-powered rover located in the southern hemisphere. As a consequence, the rover is subject to low solar power during the southern winter season, and its activities are more limited than during other seasons. For its sixth winter season Opportunity was directed to Cook Haven, a gentle swale on Murray Ridge (Fig. 4) with requisite north-facing slopes that would provide enough solar power for the rover to survive and gather some science data.

Opportunity's exploration and characterization of outcrops on Murray Ridge included imaging using Pancam and the engineering cameras, with several stops for measurements of breccia and soil targets using the MI and APXS instruments. Table 1 provides APXS compositions for Murray Ridge targets covered in this paper. Two key stops for remote sensing and compositional measurements to the north of Cook Haven were the Spinifex outcrop target and, farther south, the Moreton Island area, with its Mount Tempest and Tangalooma outcrop targets (Fig. 5). At both sites these breccia outcrops exhibit extensive fractures and contain relatively dark rock clasts several centimeters in diameter embedded in a relatively brighter, fine-grained matrix. The targets were too rough to brush or grind using the RAT.

After leaving Moreton Island, Opportunity traversed into Cook Haven from the south, thereby avoiding the need to cross south-facing slopes and low insolation values associated with the northern portion of this gentle swale. Imaging of Cook Haven shows low-lying, relatively bright outcrops cut by fractures that are partially filled with wind-blown soil deposits (Fig. 6–7). During the downhill traverse into Cook Haven Opportunity stopped on a soil-filled fracture, later executing a 146° turn, with the rear and middle wheels unintentionally excavating both the soil and underlying rocks (Figs. 7–8). Two rocks, subsequently named Pinnacle Island and Stuart Island (PI and SI), were fortuitously excavated and overturned to reveal unusually dark and bright material on the newly exposed rock surfaces. PI slid within reach of Opportunity's IDD during the drive to the Cape Elizabeth target after completing measurements on the Cape Darby outcrop, requiring no additional rover motions to deploy the MI and APXS onto the newly arrived ~3.5 cm wide rock. Opportunity conducted measurement campaigns on both PI and SI, the soil (named Anchor Point) from which they were excavated, and a loose, relatively dark rock cobble in the vicinity named Sledge Island. Bedrock outcrops Cape Elizabeth and Green Island, both flat outcrops that were brushed before MI and APXS data were acquired (Fig. 8–9), illustrate the nature of outcrops in Cook Haven in that they are relatively bright compared to other Murray Ridge outcrops, with small rock clasts set in an extensive, fine-grained matrix. On the way out of Cook Haven during the ensuing southern hemisphere spring season, Opportunity conducted measurements on one last Cook Haven outcrop, a target named Turnagain Arm, and then exited Cook Haven to continue exploring the western portion of Murray Ridge.

A breccia outcrop named Bristol Well located to the south of Cook Haven exhibited bright veins within fractures (Fig. 10). Three overlapping APXS and MI measurements were acquired to either side and centered on one of the veins. In situ measurements were also made on impact breccia targets to the south of the Bristol Well targets. These targets are the Sarcobatus outcrop matrix and two overlapping measurements on a relatively dark rock clast (Fig. 11). The matrix target was flat and smooth, enabling brushing before acquiring MI and APXS data. The last two breccia targets on Murray Ridge were Tuscaloosa and Sodaville. The former represents outcrop and the latter grus-like debris within a fracture just uphill of Tuscaloosa. After these measurements the rover continued south, conducting its last in situ measurements on a soil target named Barstow, and left Murray Ridge to begin its ascent of the Cape Tribulation rim segment (Fig. 1).

Murray Ridge outcrop and soil compositional trends

APXS compositional data in Table 1 show that Murray Ridge rocks and soils are basaltic in composition, with the notable exceptions of the Bristol Well vein and the relatively dark and bright materials associated with PI and SI rocks excavated by Opportunity's wheels. To evaluate further the extent to which there are deviations toward smectite or other phyllosilicate compositions similar to what was found on Cape York (Arvidson et al. 2014), APXS data for outcrops and soils (excluding PI and SI) are shown in a ternary plot of mole fraction Al_2O_3–($CaO+Na_2O+K_2O$)–(FeO_T+MgO) (Fig. 12). Also plotted are laboratory-based measurements for various phyllosilicates and other APXS data for Endeavour's rim. The Espérance data are for APXS measurements at Cape York in a fracture zone where progressively deeper RAT grinds showed evidence for a compositional trend toward montmorillonite (Arvidson et al. 2014). With the exception of the Bristol Well and Sledge Island measurements, no significant deviations from a narrow range of basaltic compositions are evident. Examination of data shown

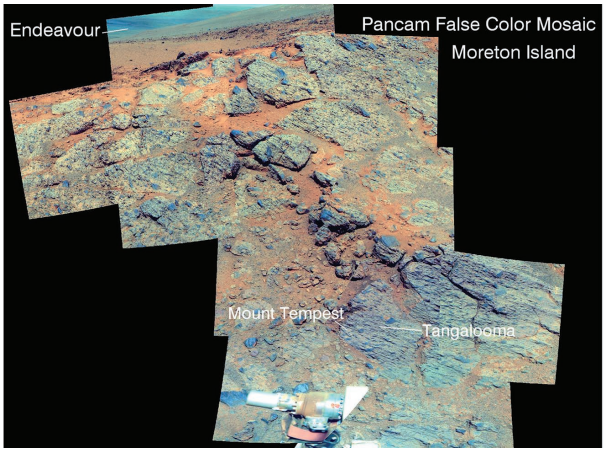

Figure 5. Pancam false color image mosaic of the Moreton Island outcrop on Murray Ridge, with the Tangalooma and Mount Tempest in situ targets shown. These highly fractured rocks are impact breccias with embedded rock clasts. For reference the outcrop with the two in situ targets is approximately 0.25 m wide. Pancam images were acquired on sols 3494–3496, with bands centered at 0.753, 0.535, and 0.432 μm shown as RGB colors. This band assignment is the same as other Pancam false color data shown in subsequent figures. Mosaic available as http://photojournal.jpl.nasa.gov/catalog/PIA17753.

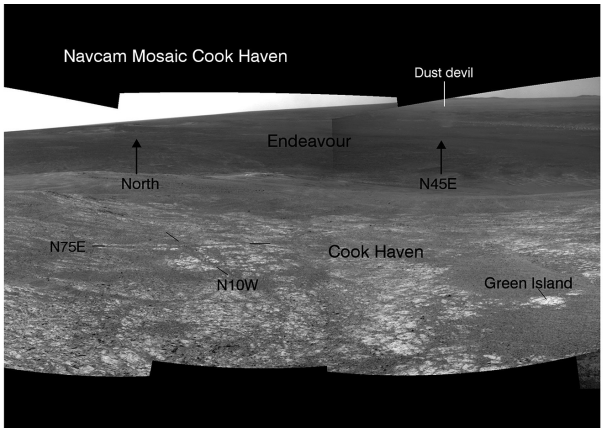

Figure 6. Navcam image mosaic acquired on sol 3512 while Opportunity was south of Cook Haven before entering this gentle swale for its winter campaign. View is to the northeast and provides an overview of the polygonally fractured, low relief outcrops that dominate Cook Haven. Two prominent fractures are shown that intersect at right angles, with strikes of N75°E and N10°W. Green Island is an in situ target for which microscopic imager (MI) and alpha particle X-ray spectrometer (APXS) data were acquired after brushing using the rock abrasion tool (RAT). For reference the Green Island outcrop is ~0.35 m wide. A dust devil can be seen on the floor of Endeavour Crater. Navcam mosaic 1NNZ12ILFCACYPDPP0673L000M2.

in Table 1 demonstrates that Sledge Island has a slightly different composition as compared to outcrops on Murray Ridge and may be an erratic added to Cook Haven (e.g., as impact ejecta).

The Bristol Well vein is ~1 cm wide and did not fill the field of view of the APXS. Three overlapping in situ measurements were made in a direction perpendicular to the vein in attempt to deter-

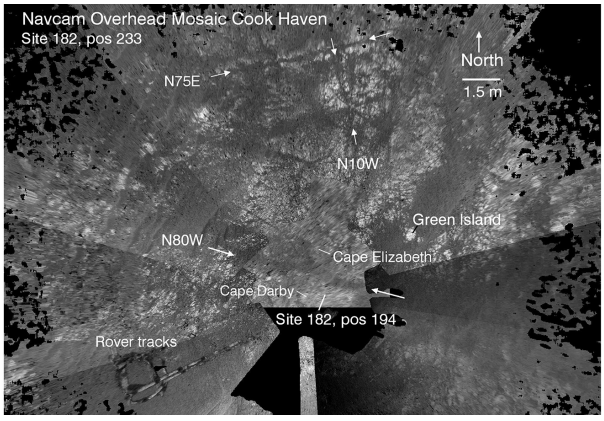

Figure 7. Orthorectified view of Navcam image mosaic shown in Figure 6, augmented with a portion from a later Navcam mosaic (Site 182, position 194, sol 3507, where site is a location where the rover coordinate system is set to zero, and position is a location relative to that new coordinate system) to show terrain elements masked by the rover in the earlier data. The two orthogonal fractures labeled in Figure 6 are shown, along with the soil-filled fracture (N80°W strike, similar in azimuth to the inferred fracture extending into Cook Haven from the west, Fig. 4) from which Opportunity excavated Pinnacle and Stuart Island rocks. The rover's turn in place and drive into Cook Haven is evident from tracks on lower left of the figure. Navcam data from site 182, position 194 are from a mosaic acquired on sol 3507, and the product ID is 1NNZ07ILFCAVRTCMP1797L000M2. Navcam data from site 182, position 233 are shown in Figure 6 in cylindrical projection whereas the orthorectified view for this figure is derived from product ID 1NNZ12ILFCAVRTDPP0673L000M2.

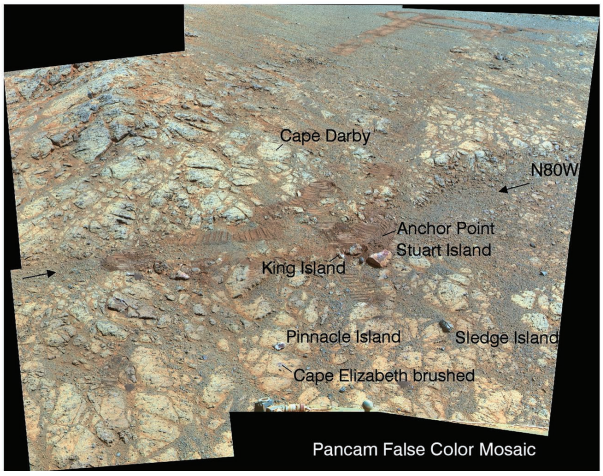

Figure 8. Pancam false color image mosaic acquired on sol 3567 from Cook Haven looking south after excavating Pinnacle and Stuart Island rocks. Also shown are in situ bedrock targets Cape Darby and Cape Elizabeth. Anchor Point in situ targets are soils excavated from the soil-filled fracture (N80°W strike), King Island is another target with a bright coating and perhaps the mate of Pinnacle Island, and Sledge Island may or may not have existed as an erratic rock before Opportunity arrived. Mosaic product IDs 1PPZ67ILFCACYLFCP2397L222M1, 1PPZ67ILFCACYLFCP2397L555M1, and 1PPZ67ILFCACYLFCP2397L777M1 were used to generate the false color mosaic. For reference Pinnacle Island is ~3.5 cm wide and Stuart Island is ~12 cm in its longest dimension.

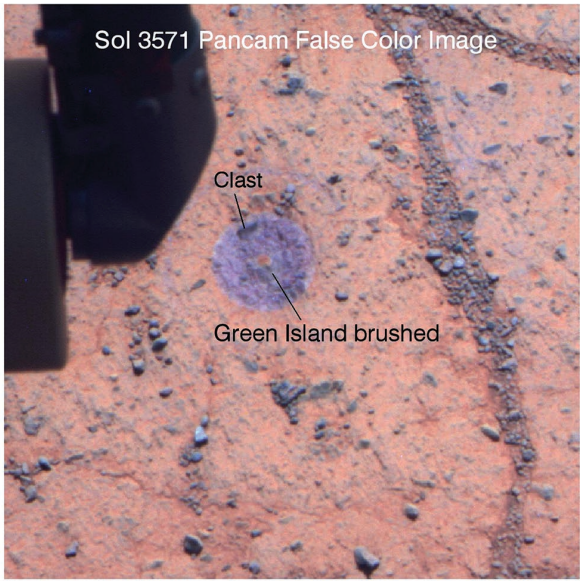

FIGURE 9. Pancam false color image of Green Island, a brushed in situ target. The brushed circle is ~3.8 cm in diameter and is dark as compared to surrounding bedrock because wind-blown dust and sand have been removed. A small rock clast can be seen embedded in the fine-grained matrix of the breccia. The central reddish spot is remnant dust and soil from the brushing activity. Soil-filled fractures are evident on the right side of the image. Generated from Product IDs 1P445203637RADCAG7P2537L2C1, 1P445203721RADCAG7P2537L5C1, and 1P445203794RADCAG7P2537L7C1.

mine vein composition, using the methodology implemented for measurements over the Homestake vein on Cape York (Squyres et al. 2012). The Bristol Well_2 target was centered over the vein and shows slightly enhanced values of Ca and S and lower values of Fe, Si, Al, and Mg as compared to Bristol Well 1 and 3 targets (Table 1). Similar compositional patterns were found for the Homestake vein that cuts the Grasberg bench deposits surrounding Cape York. Both the Homestake and Bristol Well data, and the Ortiz vein measurements on Matijevic Hill (Cape York) (Arvidson et al. 2014), indicate that sulfate-rich aqueous fluids moved through fractures and precipitated a relatively insoluble Ca sulfate mineral or minerals during one or more episodes.

The Cook Haven bedrock exposures are brighter, relatively flat-lying, and have smaller lithic clasts than other breccia outcrops on Murray Ridge. These outcrops have more S and Cl than the other breccia outcrop targets on the ridge (Fig. 13). This is the case even after brushing to remove loose dust and sand. In addition, the Sarcobatus brushed breccia matrix target shows an enrichment of Cl relative to other Murray Ridge rocks, including the Sarcobatus clast. The increase in S and Cl is interpreted to be due to the slight addition by aqueous processes of sulfate and chloride salts to selected Murray Ridge rocks, primarily to Cook Haven bedrock. The compositional trends shown in Figure 13 also highlight the very high S content of the PI and SI rocks. We consider in detail textures and compositions, together with inferred mineral phases, and explanations for the high S content of these two rocks in the next several sections of this paper.

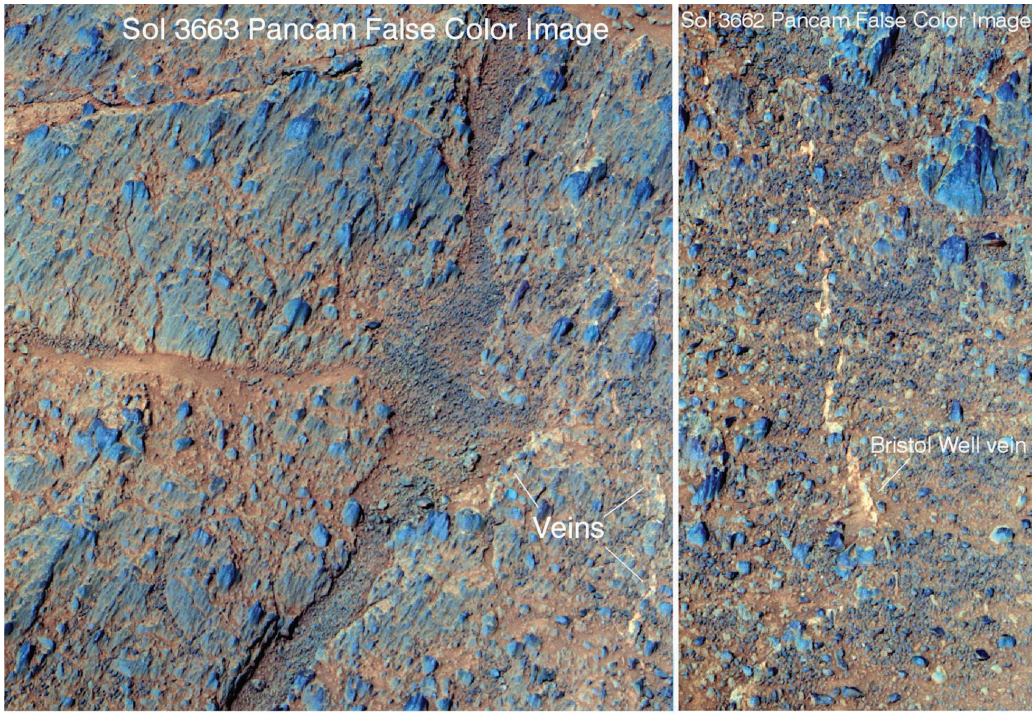

FIGURE 10. Pancam false color images of impact breccias in the Bristol Well in situ target location on Murray Ridge. Note the relatively large embedded rock clasts as compared to Green Island in Cook Haven. The **right**-hand view shows the location of the Bristol Well in situ target for which three overlapping in situ observations were acquired. This target is located to the south of the area covered by the Pancam data shown in the **left**-hand view. Table 1 shows that the compositions are consistent with the dominance of Ca-sulfate veins. For reference the large breccia block on the lower left side of the **left** image is ~0.35 m high. Portion of Pancam mosaic product IDs 1PPAG3ILFCDCYLAHP2277L222M, 1PPAG3ILFCDCYLAHP2277L555M1, and 1PPAG3ILFCDCYLAHP2277L777M1 were used to generate the **left**-hand image. Pancam product IDs 1P453282110RADCDAAP2586L2C1, 1P453282143RADCDAAP2586L5C1, and 1P453282180RADCDAAP2586L7C1 were used to generate the **right**-hand image.

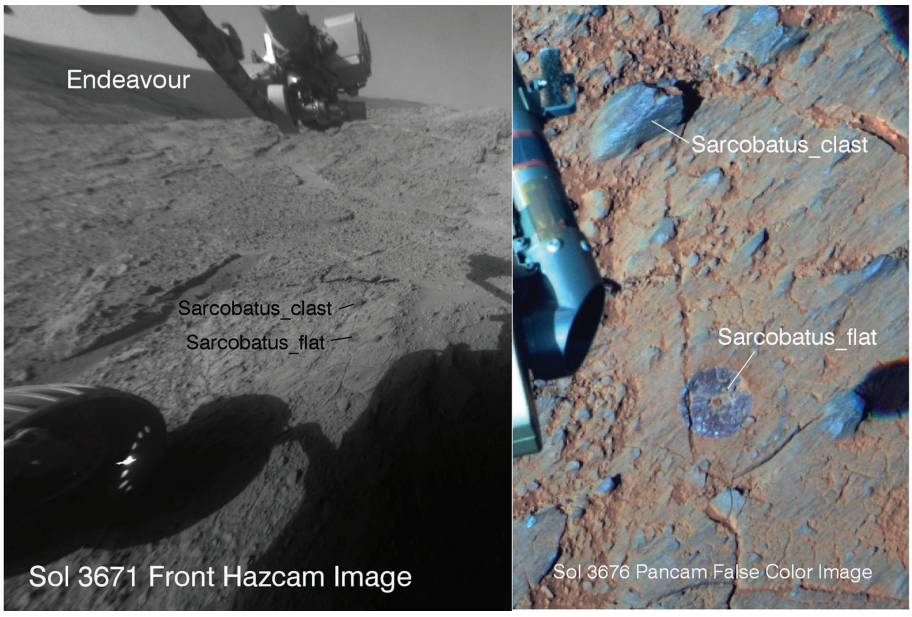

◀**FIGURE 11.** Portion of a Front Hazcam image is shown on the **left** for the Sarcobatus in situ targets for a rock clast (two overlapping measurements) and the brushed matrix target (Sarcobatus_flat). Pancam false color image of the targets is shown on the **right**. For reference the brushed spot is ~3.8 cm wide. Hazcam product ID 1F454088547FFLCDBAP1148R0M1. Pancam product IDs 1P454529822RADCDBAP2589L2C1, 1P454529907RADCDBAP2589L5C1, and 1P454529979RADCDBAP2589L7C1.

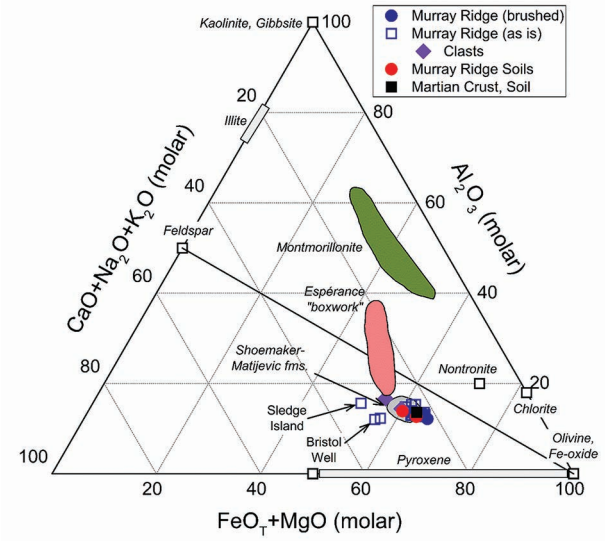

FIGURE 12. Ternary plot of mole fraction Al_2O_3–(CaO+Na_2O+K_2O)–(FeO_T+MgO) with Shoemaker and Matijevic formation data plotted for Cape York, along with Murray Ridge observations, and various phyllosilicates and pyroxene compositions. Espérance is a suite of in situ targets within a Matijevic formation fracture in which deeper grinding using the RAT and APXS observations showed a trend to montmorillonite. The Murray Ridge data lie within the field of basalts, with no evidence for alteration to phyllosilicate compositions. Montmorillonite data are from Emmerich et al. (2009) and Wolters et al. (2009).

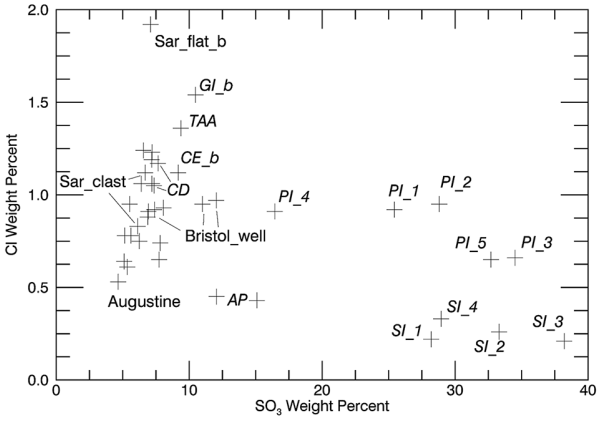

FIGURE 13. Scatter plot of S and Cl contents for APXS measurements acquired on Murray Ridge. Cook Haven data are shown in italics. Pinnacle and Stuart Island (PI and SI, respectively) measurements show large enrichments in S, with increased Cl for PI as opposed to SI measurements. The main trend shows that Cook Haven outcrops (CD = Cape Darby; CE = Cape Elizabeth; TAA = Turnagain Arm; GI_b = Green Island, brushed) are enriched in S and Cl as compared to other Murray Ridge targets. AP = Anchor Point, delineates a pair of measurements on soils dislodged by Opportunity, along with PI and SI rocks. Augustine is a rock just south of Cook Haven. Bristol Well corresponds to three measurements across a Ca sulfate vein. Sarcobatus_clast and Sarcobatus_flat_b (brushed) are targets to the south of Cook Haven. The latter is a breccia matrix enriched in Cl.

Pinnacle and Stuart Island rock coatings as observed by Pancam and the microscopic imager

Pancam false color images, together with MI anaglyphs generated from stereo observations by varying the IDD incoming angle to produce image pairs with parallax (Herkenhoff et al. 2006), show that the PI and SI rocks are thinly coated by dark materials (Figs. 14–17). In addition, PI shows evidence for a thin, bright coating interpreted to lie directly on top of relatively fresh rock surfaces and beneath the dark coating (Fig. 14–17). The dark coating is concentrated in the concave-upward center part of PI and has a lumpy texture. Pancam false color images, combined with MI data (Figs. 16–17), indicate that SI does not exhibit the same type of areally extensive, relatively bright coating found on PI. Instead in the false color images and MI data, SI exhibits an extensive and variably colored dark coating, together with areas interpreted to be relatively fresh or dusty rock surfaces. The for-

mer have a bluish-gray and the latter a reddish hue. MI anaglyphs covering SI do show several oval-shaped areas that are interpreted to be rock clasts, with one of them surrounded by a very thin, relatively bright annulus (Fig. 16). The bright annulus, in turn, is surrounded by a relatively dark annulus. Thus both PI and SI exhibit dark coatings, with a bright coating well exposed on PI.

Pancam 13-band multispectral observations (0.432 to 1.009 μm) acquired for PI, SI, and surrounding areas provide quantitative colorimetric and spectral reflectance constraints on coating mineralogy. Pancam raw image data were calibrated to surface radiance factor (I/F, where I is the measured radiance and πF is the incident solar radiance) divided by the cosine of the incidence angle at the time of image acquisition, with absolute reflectance levels accurate to within ~10% (Bell et al. 2006). Spectral end-members for PI were retrieved using the sequential maximum angle convex cone methodology in which spectral extremes are located in multi-dimensional space and separated from shadow values (Gruninger et al. 2004). Four statistically significant end-members were retrieved: relatively fresh rock, dusty rock, bright coating, and dark coating (Fig. 18).

The dusty rock end-member spectrum has a broad ferric edge absorption (~0.43–0.75 μm) interpreted to result from Fe^{3+} in nanophase iron oxides found in martian dust (Morris et al. 1993). The fresh rock end-member spectrum resembles the spectral properties of rocks on Murray Ridge not covered or only thinly covered by dust. The ferric edge is subdued relative to the dusty rock spectrum, and at longer wavelengths the spectrum shows a shallow dip, consistent with electronic absorptions due to the presence of one or more ferrous silicates, most likely pyroxene(s) (Clark 1999). The bright coating end-member has the highest reflectance values of the four PI end-members. The ferric edge is present, but not as prominent as observed for the dusty rock. The bright coating end-member spectrum also exhibits a relatively steep downturn in reflectance between 0.9 to 1.0 μm, consistent with the presence of H_2O and/or OH in the mineral structure (e.g., Rice et al. 2010).

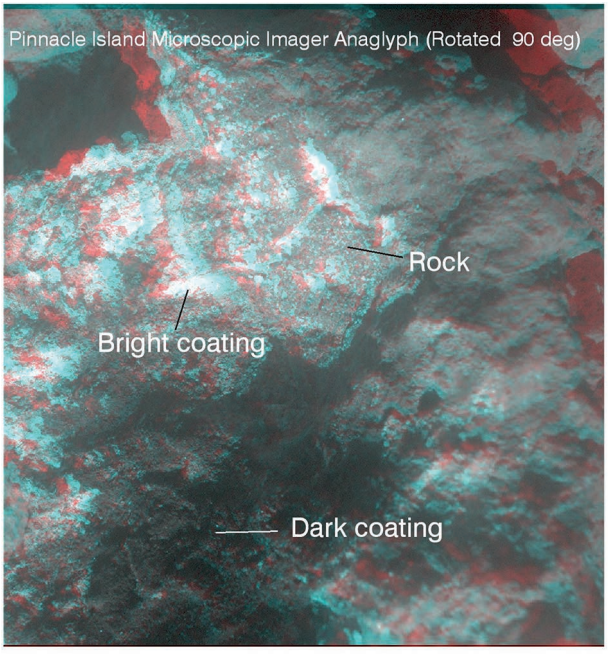

FIGURE 15. MI-based anaglyph from overlapping stereo coverage is shown for a portion of Pinnacle Island. The coating can be seen directly on top of the rock, with the dark coating occupying the center of the rock and interpreted to overlie the bright coating. The dark coating exhibits a lumpy or popcorn structure. MI product ID 1M442544805IFFCAEOP2955M2F1 and four other MI images were used to construct the anaglyph. Illumination is from the top of the scene.

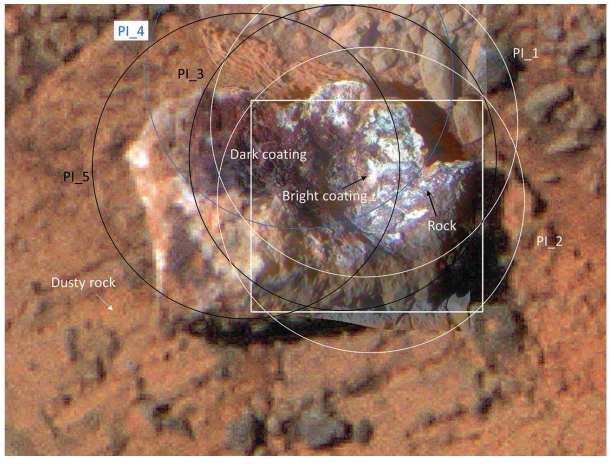

FIGURE 14. Pancam false color image acquired on sol 3541 in which the brightness has been combined with an MI mosaic of Pinnacle Island. The locations of dark and bright coatings are shown, along with dusty and fresh rock. The box shows the location of an MI-based stereo anaglyph shown in Figure 15, and the circles represent ~100% fields of view and locations for the five overlapping APXS observations. For reference Pinnacle Island is ~3.5 cm wide. Pancam product IDs 1P442541197RADCAEOP2595L2C1, 1P442541258RADCAEOP2595L5C1, and 1P442541300RADCAEOP2595L7C1. MI product ID 1M442544805IFFCAEOP2955M2F1.

Spectral end-members were retrieved using the sequential maximum angle convex cone methodology on Pancam 13-band data for SI. Four end-members were entered as a constraint, although only three could be retrieved in a statistically viable manner. The first is similar to the PI dusty rock end-member, and the second is similar to the relatively fresh rock end-member. The third is statistically indistinguishable from the PI dark coating end-member (Fig. 18). The PI and SI dark coating end-member spectra both have very low reflectance values that increase monotonically with increasing wavelength, with the exception of a shallow dip centered at 0.754 μm, and a flattening of the slope for wavelengths longer than 0.934 μm. Munsell color values (Kelly and Judd 1976) for the dark coating end-members for both rocks are 2.5R2.5/2, where 2.5R designates a slight deviation from a red hue, 2.5 indicates a dark surface, and 2 indicates a near gray appearance. The dark coating end-member color and spectral properties are unique for Mars, which ubiquitously show ferric absorptions at shorter wavelengths, increasing rapidly with increasing wavelength to ~0.77 μm, as shown for the other end-member spectra. We revisit the likely mineralogy of the dark and bright coatings after first considering constraints from the APXS-based compositions for PI and SI rocks.

Figure 16. Pancam false color image of Stuart Island acquired on sol 3567 showing the locations and 100% field of view of the four APXS observations. Box delineates location for the MI-based anaglyph shown in Figure 17. The location is denoted from which a dark area spectrum derived from Pancam data is shown in Figure 18. For reference Stuart Island is about 0.12 m in its long dimension. Pancam product IDs 1P445650967RADCAGYP2539L2C1, 1P445651052RADCAGYP2539L5C1, and 1P445651127RADCAGYP2539L7C1.

Pinnacle and Stuart Island compositions and end-member retrievals

Five overlapping APXS observations were acquired for PI (Fig. 14) and four for SI (Fig. 16) (Table 1). The field of view (FOV) of the instrument is comparable to the ~3.5 cm PI width, although most of the signal comes from the inner portion of the FOV. The situation is slightly better for the ~12 cm long SI rock. APXS placements were positioned to concentrate on the spectral end-member locations for PI and to cover the breadth of SI. For the PI APXS measurements the highly overlapping nature of the observations requires that care be taken in interpretation. Examination of the compositional data shown in Table 1 shows enrichments in Mg, Mn, Ni, and S for both PI and SI, relative to surrounding basaltic bedrock. The enrichment patterns are also distinctly different than found for the sulfate-rich sandstones that dominate the Burns formation (Clark et al. 2005). The APXS FOVs containing the highest concentrations of the dark coating end-member (PI_3, PI_5) have the greatest enrichments in these elements. PI_3 and PI_5 also show minor enrichments in Ca and P, and overall the PI targets have higher concentrations of Cl, relative to SI targets (Fig. 13, Table 1). PI_3 has the highest concentration of Mn (3.48 wt% MnO, Table 1) measured thus far by the Spirit and Opportunity rovers, and SI_3 has the highest S concentration (38.21 wt% SO_3, Table 1) measured by either rover. PI and SI coating compositions are thus unique among the many hundreds of APXS measurements collected by the Spirit and Opportunity rovers (Gellert et al. 2006).

Because the APXS FOV is large relative to the size of PI, it is not possible to use the observations alone to retrieve the compositions of the purest dark and bright coatings that are well-exposed on this rock and localized using Pancam spectral analysis. On the other hand, if we assume that the compositions follow the areal concentrations of Pancam-based end-members, various techniques can be used to retrieve compositional estimates for the purest end-member locations. To pursue these retrievals, the location of each APXS PI measurement was derived from examination of MI frames pointed toward the APXS target center, together with projections of the IDD motions toward the target. Locations were refined using the predicted total signal as a function of terrain topography and derived APXS stand-off distances. Overall the methodology for localization of the APXS measurements followed the procedures described in VanBommel et al. (2016).

For each PI APXS observation the Pancam-based end-member phase abundance maps were spatially convolved with the APXS FOVs at the Pancam pixel scale, given the APXS measurement location, the lateral distance from the detector center, the APXS detector stand-off distance, and topography (Fig. 19). To ensure more observations than unknowns in retrieving compositions for the Pancam-based purest end-member locations, the dusty and fresh rock end-members were combined, and SI, Anchor Point soils, and Cook Haven bedrock observations were added to the data matrix. Thus, 16 measurements were used together with the phase abundance matrix (3 end-member columns and 16 observation rows) to solve for the compositions of 3 end-members (16 oxide columns and 3 end-member rows): rock, bright coating, and dark coating. In matrix notation the phase abundance matrix was post-multiplied by the end-member composition matrix to generate the matrix of oxide compositions.

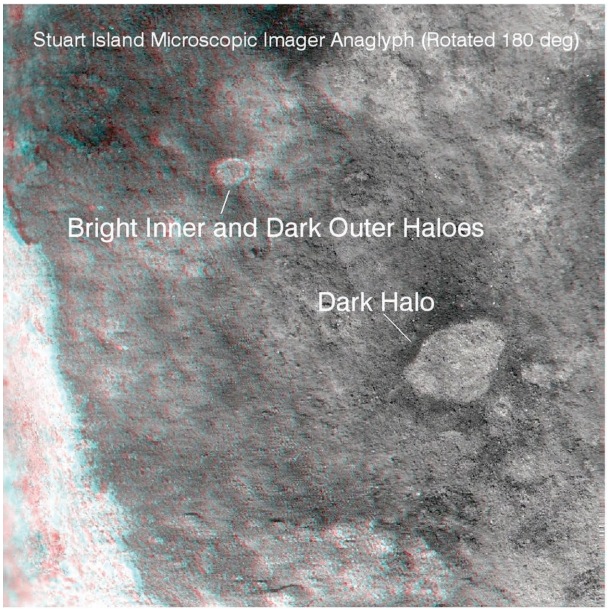

Figure 17. MI-based anaglyph of a portion of Stuart Island that shows a thin bright annulus around what is interpreted to be a rock clast. This bright annulus is surrounded by a dark coating. A second clast is surrounded by a dark coating. MI product ID 1M445651708IFFCAGYP2935M2F1 and four other MI frames were used to construct the anaglyph. Target was fully shadowed when the data were acquired.

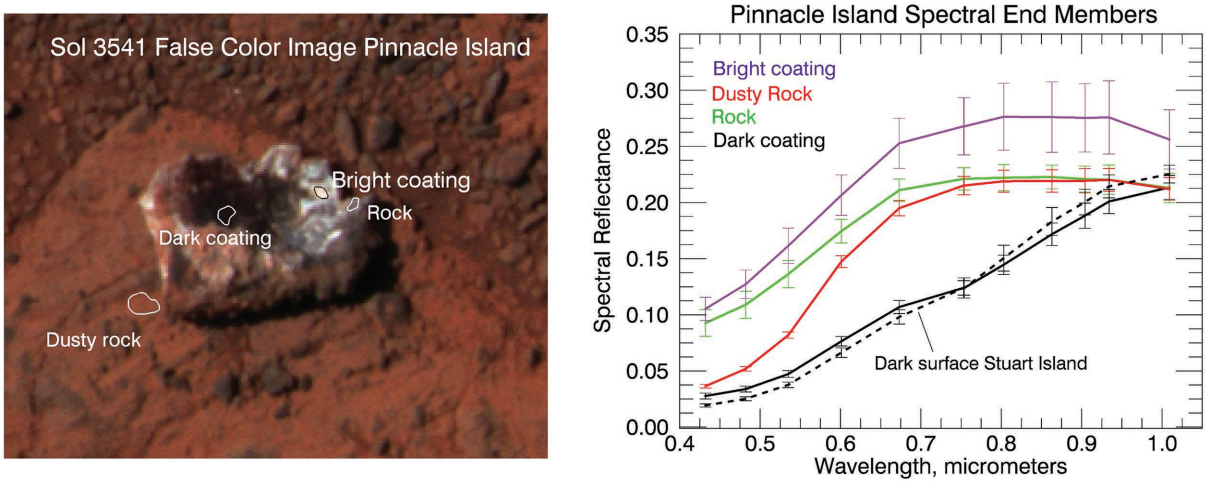

FIGURE 18. Locations of Pancam spectral end-members derived from the unmixing algorithm are shown on the Pancam false color image on the **left**, and mean spectra for these regions are shown on the **right**. Also shown is the mean spectrum for the dark area on Stuart Island. One standard deviation error bars are also plotted. The dark coating spectra for the Island rocks are indistinguishable and unique for any Pancam observation. The spectra lack the ferric absorption edge shortward of ~0.7 μm that is characteristic of martian spectra, and evident for the other three spectra shown in the figure. The dusty rock spectrum has the deepest ferric absorption edge, followed by the bright coating spectrum, and the rock spectrum has the shallowest absorption.

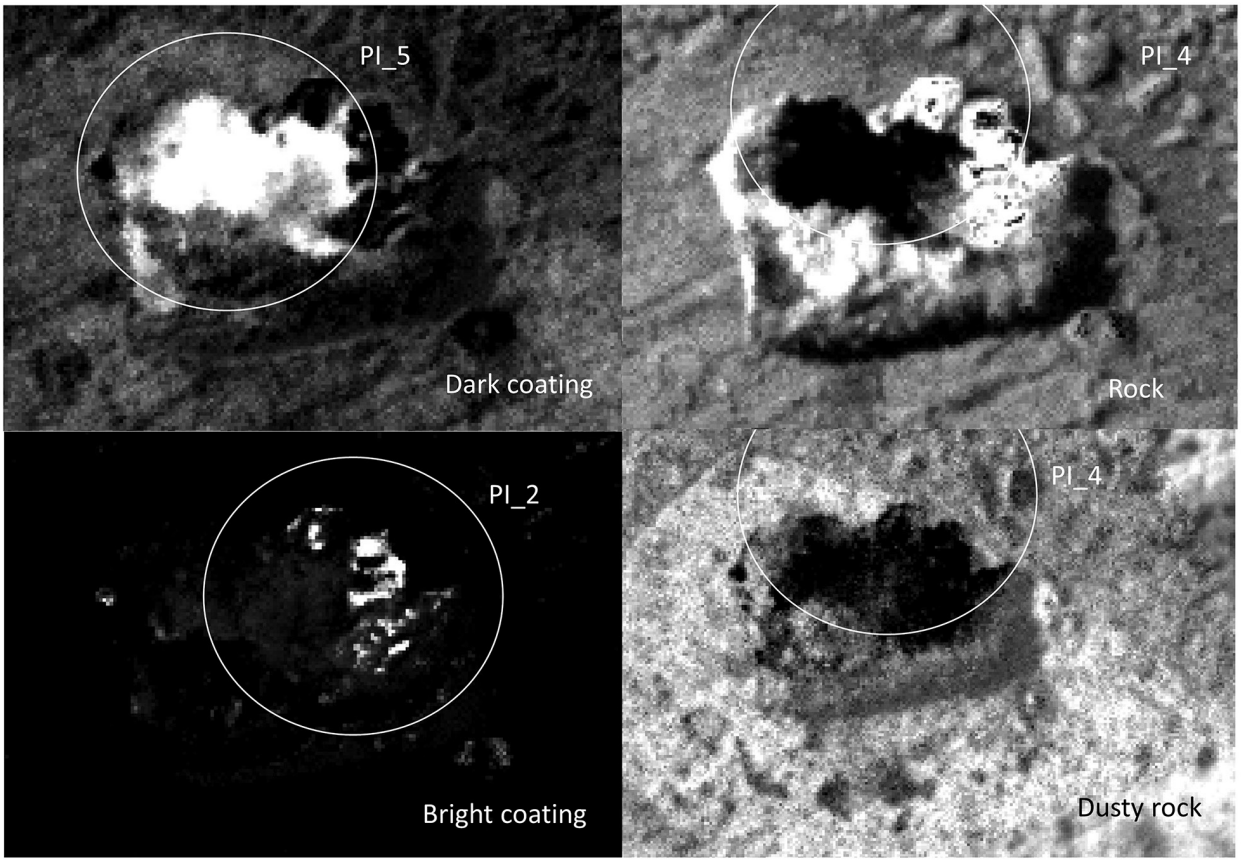

FIGURE 19. Pinnacle Island end-member concentration maps for dark and bright coatings, fresh rock, and dusty rock are shown, along with APXS fields of view that correspond to the highest retrieved areal concentrations of each of these end-members (Table 3). As discussed in the text the dusty and fresh rock end-members were combined to a single rock end-member in the retrievals.

An iterative minimization algorithm with a non-negativity constraint was used in which both the phase abundance and end-member composition matrix values were allowed to vary. Initial phase abundances for PI observations were set by the Pancam-based end-member map convolutions with the APXS FOVs, whereas the other initial phase abundances were initially set to random numbers, including those for SI. The sums of squared deviations between the model predictions and measured values for the 16 elements for the 16 APXS measurements were minimized and used to compute statistical errors of the retrieved end-member compositions and phase abundances. Results are presented in Table 2 for retrieved end-member compositions and Table 3 for phase abundances. Major elements were retrieved with small errors for the dark coating and rock end-members. The bright coating end-member composition retrievals have relatively large errors that are a consequence of the small areal extent of this end-member and thus relatively poor APXS statistics. Low concentration elements were also difficult to retrieve for all end-members and some zero values were retrieved, which is compositionally incorrect, and a limitation of the retrieval procedure. Phase abundance retrievals are consistent with the Pancam-based images for PI; e.g., examinations of APXS locations over the end-member abundance maps are consistent with retrievals shown in Table 3. In addition, SI phase abundances show high concentrations of bright and dark end-members in all four observations, consistent with the more complicated color patterns evident in Pancam data for SI than for PI (Figs. 14 and 16).

To pursue how the end-member retrievals match and/or extend trends in compositions, a correspondence analysis (CA) was run for all measurements on Murray Ridge and included the three end-member compositions (Fig. 20). CA is a row- and column-normalized principal component analysis used for understanding correlations among samples and variables and has been used to explore patterns for the intrinsically multivariate APXS data acquired by both the Spirit and Opportunity rovers (Arvidson et al. 2010, 2011). The first two CA factor loadings, which carry ~98% of the data variance, demonstrate that the rock end-member composition has a close affinity to bedrock. The bright and dark coating end-members extend the differences in compositions between the measurements centered over the bright and dark coating exposures on PI. The bright coating end-member is characterized by an affinity for magnesium and sulfur, and modest amounts of manganese, whereas the dark coating also has an affinity for manganese, calcium, and phosphorus, in addition to magnesium and sulfur.

We also use the trends evident in the CA factor loadings plot to consider bivariate correlations between oxide compositions; e.g., Si and S are clearly negatively correlated (Fig. 20). This correlation is evident in a plot of the two oxides and by the high correlation coefficient of these two elemental abundances (Fig. 21). Mg and S are positively correlated as are Ca and P (Figs. 20–21). The retrieved rock and dark coating end-members set upper and lower bounds on the first three bivariate plots, whereas the Ca vs. P plot shows a much greater spread of data and end-members. Ni is not well estimated in the end-member retrievals. However, a strong Mn vs. Ni positive correlation is evident in the bivariate plot shown in Figure 22, using only the actual APXS observations.

TABLE 2. Compositions and associated errors for Pinnacle Island end-members in weight percent for each oxide

	Abundance (wt%)			Error (wt%)		
	Dark	Bright	Rock	Dark	Bright	Rock
SiO_2	0.42	27.03	47.90	1.25	10.80	0.86
TiO_2	0.07	0.83	1.15	0.10	0.25	0.03
Al_2O_3	0.00	5.48	9.66	0.00	2.12	0.01
Cr_2O_3	0.00	0.22	0.28	0.02	0.08	0.01
FeO	14.64	17.64	17.35	0.73	0.99	0.22
MnO	5.41	1.38	0.00	0.18	1.39	0.06
MgO	16.5	14.26	6.60	0.61	1.83	0.16
CaO	7.89	2.11	6.62	0.70	1.53	0.30
Na_2O	0.00	0.71	2.46	0.00	0.43	0.06
K_2O	0.00	0.15	0.46	0.00	0.07	0.01
P_2O_5	3.27	0.00	1.07	0.31	0.49	0.12
SO_3	51.42	30.07	5.15	2.06	10.14	1.02
Cl	0.31	0.00	1.23	0.29	0.10	0.08
Ni	767	941	407	883	739	159
Zn	0	177	216	28	116	38
Br	14	74	206	178	81	51

TABLE 3. End-member abundances for APXS observations, with numbers in percent for each end-member and estimated errors

	Abundance (%)			Error (%)		
	Dark	Bright	Rock	Dark	Bright	Rock
CapeDarby	4	2	94	4	5	3
CapeDarby2	5	2	93	5	6	3
CapeElizabeth	5	7	88	5	9	6
PinnacleIsland1	38	9	53	3	1	3
PinnacleIsland2	40	11	50	3	3	1
PinnacleIsland3	56	5	38	2	2	1
PinnacleIsland4	23	5	72	2	1	2
PinnacleIsland5	64	1	35	5	2	6
GreenIsland	4	8	88	4	12	7
StuartIsland1	22	49	29	14	15	11
StuartIsland2	22	69	9	22	15	12
StuartIsland3	40	58	2	22	16	6
StuartIsland4	34	41	25	12	11	10
AnchorPoint1	13	17	70	7	16	9
AnchorPoint2	12	14	74	12	24	12
TurnagainArm	3	10	87	4	9	6

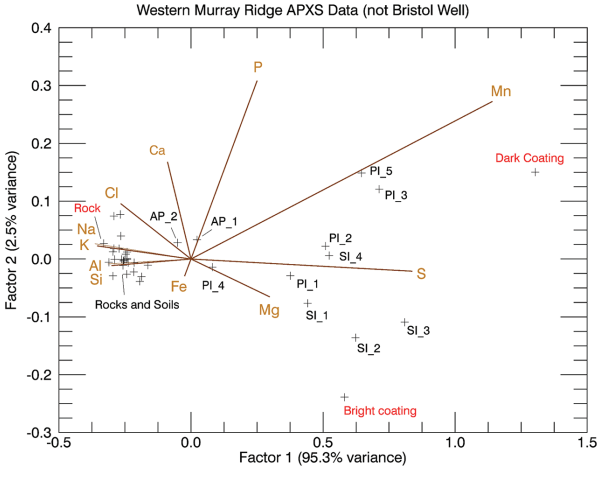

FIGURE 20. Correspondence analysis for the first two factor loadings is shown for Murray Ridge observations, except for the three Bristol Well Ca sulfate vein measurements. Also included in the calculations were the three Pinnacle Island-based end-members (rock, dark coating, and bright coating), which on the plot extend beyond, but encapsulate the data. The end-members show the affinity of the dark coating for Mn, S, P, and Ca, whereas the bright coating end-member shows an affinity for Mg and S.

Inferred Pinnacle Island bright and dark coating mineral phases

The bright end-member coating spectral reflectance is consistent with the presence of a pure Mg-sulfate end-member, although the composition, low overall reflectance relative to Mg sulfate powders and rocks (e.g., Cloutis et al. 2006), and the presence of the short-wavelength ferric absorption imply a more complex mineral assemblage. The dark coating end-member spectral characteristics are clearly indicative of the presence of one or more minerals that are intrinsically dark because of multiple, overlapping charge transfer and/or electronic transition absorptions associated with the presence of transition metals such as Mn (Sherman 1984). We explore a range of possible candidates to show that the low reflectance and lack of ferric edge are consistent with the presence of Mn oxides. Several synthetic samples were generated and used to pursue this comparison, including hausmannite [$(Mn^{2+},Mn^{3+})_2O_4$], bixbyite (α-$Mn_2^{3+}O_3$), pyrolusite (β-$Mn^{4+}O_2$), and a series of phyllomanganates: triclinic and hexagonal forms of birnessite [$(Na,Ca,K)_x(Mn^{4+},Mn^{3+})_2O_4{\cdot}nH_2O$)], and vernadite ($Na_{0.2}Mn^{4+}_{0.95}O_2{\cdot}nH_2O$). These phases were synthesized in the laboratory under controlled conditions, with phase identification verified using X-ray diffraction (Hinkle 2015). Spectral reflectance data were acquired for silt-sized portions of these minerals with lighting and viewing conditions similar to those for which the Pancam data were acquired (Fig. 23). All of the Mn oxide spectra have low overall values and either are spectrally flat, or increase modestly in reflectance with increasing wavelength, consistent with the overlapping nature of the charge transfer and electronic transition absorptions for these oxides. To our knowledge no other Mn-bearing minerals (e.g., Mn sulfates, which are bright pink) exhibit these spectral characteristics. Mn sulfides were not considered to be viable matches for the dark coating end-member spectra because these minerals are exceptionally rare in nature. The reason is that the electronic structure of Mn favors the maintenance of localized 3d orbitals in a high-spin configuration, rather than hybridization into molecular orbitals shared with sulfur and typical of other sulfide minerals (Vaughan and Rosso 2006).

To further pursue possible mineral assemblages we calculated the phases that would have been produced if the bright and dark coating end-member compositions formed via equilibrium precipitation from an aqueous fluid. Calculations were based on a geochemical reaction model using The Geochemist's Workbench version 10.0.6 (Bethke 2007). Oxide components reported in

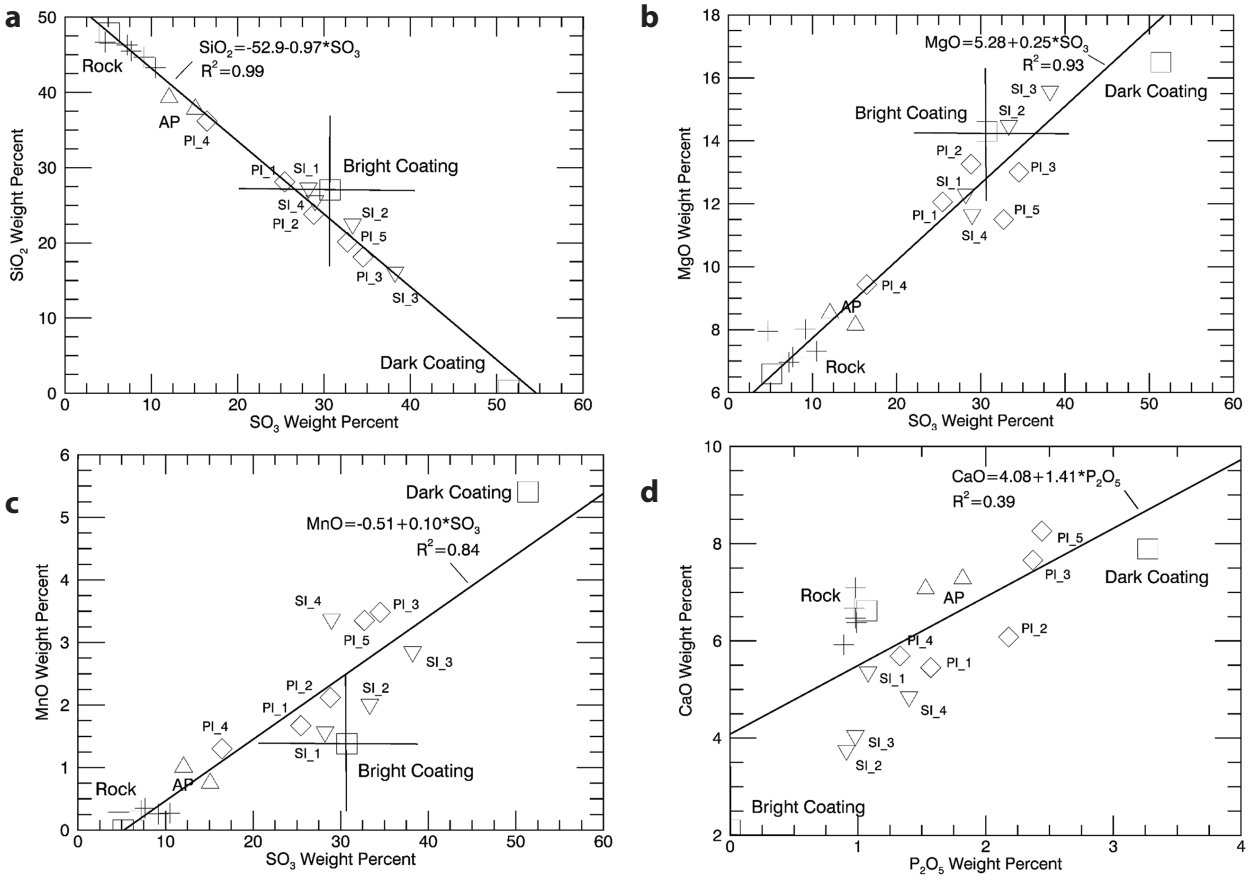

FIGURE 21. Bivariate plots are shown of SiO_2, MgO, and MnO as a function of SO_3 contents, along with CaO as a function of P_2O_5, for Cook Haven APXS measurements. Bright and dark coatings and rock retrieved end-member compositions are also shown. Error bars are plotted for the bright coating (Table 2). For the other two end-members the errors are comparable to the box symbol sizes. Least-squares linear fits to the APXS data (not end-members) are shown as straight lines, along with the square of the Pearson linear correlation coefficient. These bivariate plots were chosen to illustrate trends with high correlation coefficients, based on results from the correspondence analysis shown in Figure 20.

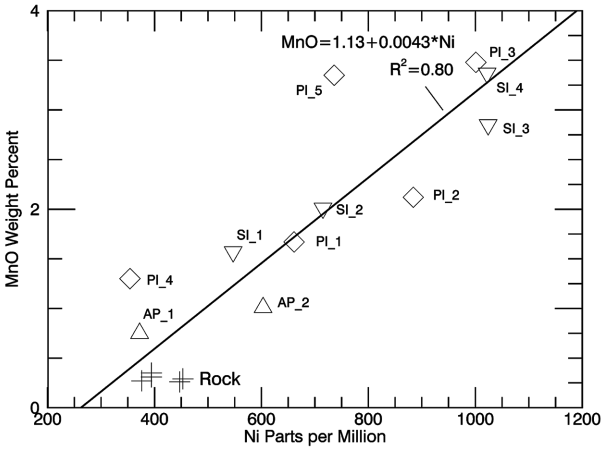

FIGURE 22. MnO vs. Ni bivariate plot is shown for Cook Haven outcrops, Anchor Point soils, and Pinnacle and Stuart Islands. Least-squares linear fits to the data are shown as straight lines, along with the square of the Pearson linear correlation coefficient.

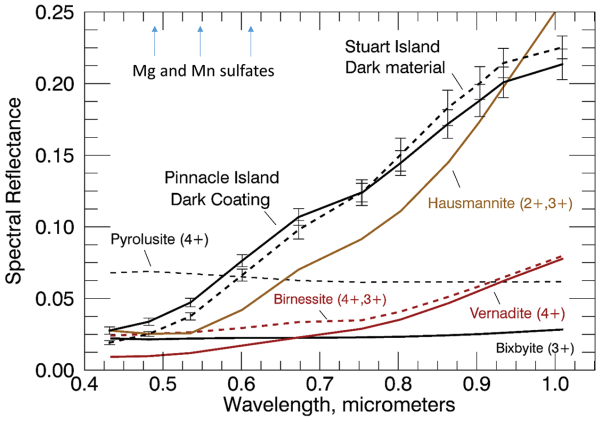

FIGURE 23. The Pinnacle Island dark coating end-member spectrum is shown, together with data from the region with the highest concentration of this end-member mapped to Stuart Island. Data are also shown for lab spectra of synthesized Mn oxides. Mg- and Mn-bearing sulfates have much brighter spectra as shown by the labels and arrows at the top of the plot. Only high valence state Mn oxides are compatible with the spectral trends observed in the dark areas on the two Island rocks and the compositions of these two targets. A unique mineral phase is impossible to retrieve, given the number of unknowns (optical constants, grain size, and shape of each constituent, together with coating porosity) involved in any retrievals, together with the limited Pancam spectral range and number of bands.

Table 2 were modeled as reacting with 1 kg of water, converting to mineral phases based on fluid saturation state. Cr_2O_3, Br, Ni, and Zn were excluded from the model as these occur at minor to trace levels and will largely occur as substituting elements in other minerals. Reaction of 1.5 kg of oxide components with 1 kg of water yielded a stable configuration, i.e., an incremental addition of oxide components yielded a proportional increase in existing minerals. This reaction left a residual brine containing primarily Mg and sulfate; this fluid was then evaporated to obtain the full mineralogy. The initial reaction employed a previously described thermodynamic database (Catalano 2013). The evaporation step required use of a Pitzer-style activity model. A previously compiled database (Tosca et al. 2005, 2007) was modified with more recent compilations of ion-interaction parameters (Marion et al. 2003, 2008, 2009, 2010) and revised solubility data (Grevel and Majzlan 2009, 2011; Kobylin et al. 2011; Majzlan et al. 2004a, 2004b). Pitzer models are not parameterized for P and Ti, and thus these elements were removed for the evaporation step; >99.99% of the P and Ti added to the system were precipitated in minerals in the initial reaction. All calculations were performed at 25 °C because the thermodynamic data available are most robust at this temperature.

The geochemical modeling results yield plausible mineral assemblages, with both end-members dominated by Mg sulfate, as expected from the bulk compositions (Fig. 24). The dark coating end-member retrieval also contains gypsum, ferric hydroxysulfates, and ferric phosphate, with the bright coating retrieval containing nontronite (as the main host of SiO_2), and minor gibbsite and gypsum. Mn in both coatings is predicted to occur as a phyllomanganate (birnessite), with the dark coating containing a substantially larger mass fraction of this mineral. These calculations assume all phases were in equilibrium and that the end-members contained no detrital material. Neither assumption is fully valid for real systems. Thus these calculated assemblages simply demonstrate that end-member compositions correspond to realistic mineral assemblages that would form by precipitation from aqueous solutions. Additional calculations (not shown) explored possible paragenetic sequences associated with closed system chemical processes during and after deposition, but were unable to produce the dark coatings by alteration or leaching of the bright coatings, and vice versa, as both contain mixtures of soluble and insoluble phases and have distinct compositions. The model results suggest that the formation of these coatings involved multiple stages of fluid flow and coating formation.

Formation and uniqueness of Pinnacle and Stuart Island coatings

The morphologic, stratigraphic, spectral, and compositional patterns evident on the PI and SI rock surfaces are interpreted to indicate two episodes of authigenic mineral deposition, both dominated by precipitation of sulfates from subsurface fluids that were largely neutralized by reactions with basaltic bedrock. The initial precipitation generated bright coatings that were subsequently altered to form a thin layer of what is likely Mg-sulfate-dominated mineralogy that also includes Mn oxides. We note that the presence of Mn oxides would also suggest scavenging of Ni (Post 1999), thereby helping to explain the positive correlation between these two elements (Fig. 22). The precipitation of Mn oxides requires the presence of a high concentration of potential oxidants (e.g., O_2, although this is by no means a unique identification), most likely associated with fluids in direct contact with the atmosphere. To account for the observed elemental correlations, incorporation of Ca, P, Cl, and Br into one or more phases [e.g., chloroapatite (Klein 2002)] must also have occurred for PI.

The PI and SI coating compositions are unique among the many hundreds of APXS measurements acquired by the Op-

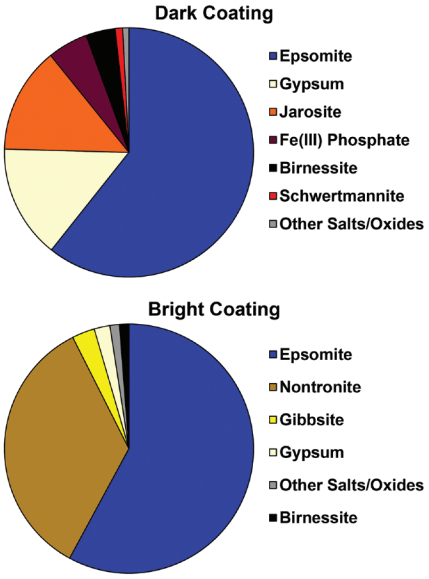

FIGURE 24. Mass fractions of minerals produced by equilibrating the end-member coating compositions (Table 2) with water in a geochemical reaction model. The "Other Salts/Oxides" category contains rutile and an array of minor sulfate and chloride salts.

portunity and Spirit rovers. This is evident in a plot of Fe vs. Mn for all data collected through Murray Ridge (Fig. 25). It is also evident when the S- and Cl-free PI and SI compositions are placed in context with all of the soil and bedrock measurements. Specifically, projecting the data onto an S- and Cl-free ternary diagram illustrates the decreasing importance of silicates and Fe-bearing phases as PI and SI measurements move from rock to bright coating to dark coating compositions (Fig. 26). PI and SI coating trends are distinctly different from trends related to hematitic concretions in the Burns formation sulfate-rich sandstones (Morris et al. 2006), Ca-sulfate veins on Cape York and surrounding bench deposits (Squyres et al. 2012), Bristol Well Ca-sulfate veins, and aluminous phyllosilicates (Espérance) in a fracture on Cape York (Arvidson et al. 2014).

IMPLICATIONS

Endeavour's highly fractured rim is interpreted to have provided a conduit for subsurface fluid flow, and this would have particularly been the case in the immediate aftermath of the crater-forming impact event and associated heating of groundwater (e.g., Osinski and Pierazzo 2012). Based on Opportunity observations, most of the impact breccia outcrops on the western rim of Endeavour's Murray Ridge rim segment do not show major element compositional deviations from a basaltic composition. Minor fracture-filling Ca-sulfate veins have been encountered, implying modest flow of fluids and regional-scale precipitation of a relatively insoluble sulfate phase or phases. In addition, relatively high S and Cl concentrations associated with Cook Haven bedrock outcrops imply modest addition of these mobile elements. On the other hand, Pinnacle and Stuart Island rocks, serendipitously excavated from a soil-filled fracture by Opportunity's wheels, provide strong evidence for movement of fluids through the subsurface, and formation of a unique sulfate-

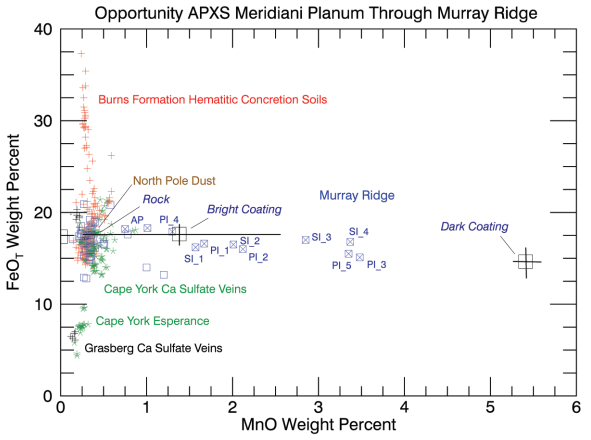

FIGURE 25. Fe and Mn concentrations are plotted for all of Opportunity's APXS observations through Murray Ridge, together with the three end-member values retrieved from Pinnacle Island data. The trends for the Island rocks are unique and indicate a special process that concentrated Mn relative to Fe in the bright and, especially, the dark coatings.

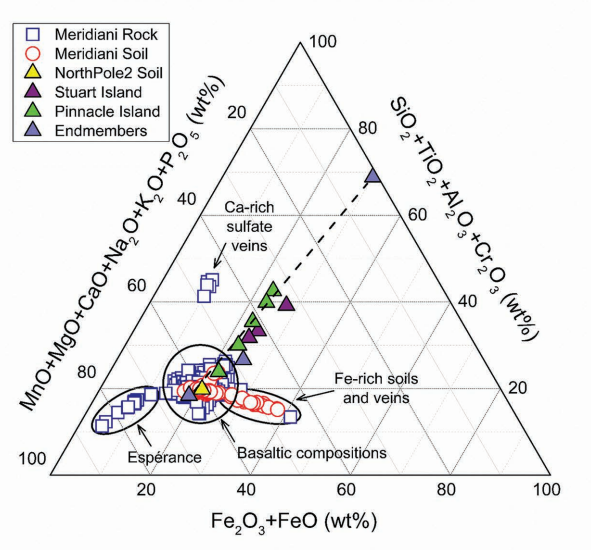

FIGURE 26. Ternary plot for all Meridiani Planum and Endeavour Crater soil and bedrock APXS analyses through measurements acquired on Murray Ridge and calculated to SO_3 = Cl = 0.0 wt%. The trends show the unique chemistry of Pinnacle and Stuart Island targets as compared to other rock and soil compositions and are broadly consistent with precipitation from aqueous sulfate solutions. The dashed arrow terminates on the extrapolated SO_3-free composition of the mixed-cation sulfate-dominated end-member, which is also the location of the predicted dark coating end-member. The rock end-member plots within the rock and soil field, whereas the bright coating end-member plots between the other two end-members, slightly displaced toward the Fe apex. This trend is consistent with the ferric edge observed in the spectrum for this end-member and the inferred presence of one of more Fe^{3+}-bearing phases. North Pole_2 is a dust-covered soil target measured by Opportunity on the Cape York rim segment of Endeavour Crater. This target has a composition that is representative of martian global dust and plots near the center of the cluster. Fe-rich soils are concentrations of hematitic concretions eroded from the Burns formation.

rich deposit overlain by a sulfate and Mn oxide-rich coating.

On the basis of inferred mineralogy, the aqueous fluids that deposited coatings on Pinnacle and Stuart Island rocks exhibited temporally varying redox conditions governed by subsurface rock-water interactions in contact with an oxidizing surface environment. Discovery of these rare deposits on the rim of Endeavour Crater complements the discovery of equally rare Mn-oxide deposits formed by aqueous flow in subsurface fractures by the Curiosity rover in Gale Crater (Lanza et al. 2015). These two discoveries demonstrate that Mn-oxides must have been part of the planet's secondary mineral repertoire that required a stronger redox gradient in some near-surface environments than previously recognized. In contrast to arid regions on Earth, where Mn oxides are widely incorporated into coatings on surface rocks (e.g., Liu and Broecker 2008), our results demonstrate that on Mars the most likely place to deposit and preserve Mn oxides was in fracture zones where migrating fluids intersected surface oxidants, forming precipitates shielded from subsequent physical erosion.

Acknowledgments

We thank the Opportunity Project Team at the NASA/Caltech Jet Propulsion Laboratory and scientists from many institutions who made possible the collection of data included in this paper. We thank Paolo Bellutta for help in localizing APXS fields of view and Susan Slavney and Jennifer Ward for careful review and editing of text and figures. Bonnie Redding, U.S. Geological Survey, kindly generated the MI anaglyphs. We also thank NASA for the support needed to operate Opportunity and collect and analyze the data included in this paper and the Mars Fundamental Research Program support to J.G. Catalano. The NASA Planetary Data System Geosciences Node houses the data included in this paper and we thank them for their efforts. See http://pds-geosciences.wustl.edu/. Any use of trade, firm, or product names is for descriptive purposes only and does not imply endorsement by the U.S. Government.

References cited

Arvidson, R.E., Bell, J.F. III, Bellutta, P., Cabrol, N.A., Catalano, J.G., Crumpler, L., Des Marais, D.J., Estlin, T., Farrand, W., Gellert, R., and others. (2010) Spirit Mars Rover mission: Overview and selected results from the northern Home Plate Winter Haven to the side of Scamander crater. Journal of Geophysical Research: Planets, 115, E00F03, doi:10.1029/2010JE003633.

Arvidson, R.E., Ashley, J.W., Bell, J.F. III, Chojnacki, M., Cohen, J., Economou, T.E., Farrand, W.H., Fergason, R., Fleischer, I., Geisler, P., and others. (2011) Opportunity Mars Rover mission: Overview and selected results from Purgatory ripple to traverses to Endeavour crater. Journal of Geophysical Research: Planets, 116, E00F15, doi:10.1029/2010JE003746.

Arvidson, R.E., Squyres, S.W., Bell, J.F., Catalano, J.G., Clark, B.C., Crumpler, L.S., de Souza, P.A., Fairén, A.G., Farrand, W.H., Fox, V.K., and others. (2014) Ancient aqueous environments at Endeavour crater, Mars. Science, 343, doi:10.1126/science.1248097.

Bell, J.F., Squyres, S.W., Herkenhoff, K.E., Maki, J.N., Arneson, H.M., Brown, D., Collins, S.A., Dingizian, A., Elliot, S.T., Hagerott, E.C., and others. (2003) Mars Exploration Rover Athena Panoramic Camera (Pancam) investigation. Journal of Geophysical Research: Planets, 108, 8063, doi:10.1029/2003JE002070.

Bell, J.F. III, Joseph, J., Sohl-Dickstein, J.N., Arneson, H.M., Johnson, M.J., Lemmon, M.T., and Savransky, D. (2006) In-flight calibration and performance of the Mars Exploration Rover Panoramic Camera (Pancam) instruments. Journal of Geophysical Research, 111, E02S03, doi:10.1029/2005JE002444.

Bethke, C.M. (2007) Geochemical and Biogeochemical Reaction Modeling, 547 p. Cambridge University Press, New York.

Catalano, J.G. (2013) Thermodynamic and mass balance constraints on iron-bearing phyllosilicate formation and alteration pathways on early Mars. Journal of Geophysical Research: Planets, 118, 2124–2136, doi:10.1002/jgre.20161.

Clark, R. (1999) Chapter 1: Spectroscopy of rocks and minerals, and principles of spectroscopy. In A.N. Rensz, Ed., Remote Sensing for the Earth Sciences, 3, pp. 3–58. Wiley, New York.

Clark, B.C., Morris, R.V., McLennan, S.M., Gellert, R., Jolliff, B., Knoll, A.H., Squyres, S.W., Lowenstein, T.K., Ming, D.W., Tosca, N.J., and others. (2005) Chemistry and mineralogy of outcrops at Meridiani Planum. Earth and Planetary Science Letters, 240, 73–94, doi:10.1016/j.epsl.2005.09.040.

Cloutis, E.A., Hawthorne, F.C., Mertzman, S.A., Krenn, K., Craig, M.A., Marcino, D., Methot, M., Strong, J., Mustard, J.F., Blaney, D.L., Bell, J.F. III, and Vilas, F. (2006) Detection and discrimination of sulfate minerals using reflectance spectroscopy. Icarus, 184, 121–157, doi:10.1016/j.icarus.2006.04.003.

Crumpler, L.S., Arvidson, R.E., Bell, J., Clark, B.C., Cohen, B.A., Farrand, W.H., Gellert, R., Golombek, M., Grant, J.A., Guinness, E., and others. (2015) Context of ancient aqueous environments on Mars from in situ geologic mapping at Endeavour Crater. Journal of Geophysical Research: Planets, 120, 538–569, doi:10.1002/2014JE004699.

Ehlmann, B.L., and Edwards, C.S. (2014) Mineralogy of the Martian surface. Annual Review of Earth and Planetary Sciences, 42, 291–315, doi:10.1146/annurev-earth-060313-055024.

Emmerich, K., Wolters, F., Kahr, G., and Lagaly, G. (2009) Clay profiling: The classification of montmorillonites. Clays and Clay Minerals, 57, 104–114.

Gellert, R., Rieder, R., Brückner, J., Clark, B.C., Dreibus, G., Klingelhöfer, G., Lugmair, G., Ming, D.W., Wänke, H., Yen, A., and others. (2006) Alpha Particle X-ray Spectrometer (APXS): Results from Gusev crater and calibration report. Journal of Geophysical Research: Planets, 111, E02S05.

Gorevan, S.P., Myrick, T., Davis, K., Chau, J.J., Bartlett, P., Mukherjee, S., Anderson, R., Squyres, S.W., Arvidson, R.E., Madsen, M.B., and others. (2003) Rock Abrasion Tool: Mars Exploration Rover mission. Journal of Geophysical Research: Planets, 108, 8068.

Grant, J.A., Parker, T.J., Crumpler, L.S., Wilson, S.A., Golombek, M.P., and Mittlefehldt, D.W. (2015) The degradational history of Endeavour Crater, Mars. Icarus, in press, doi:10.1016/j.icarus.2015.08.019.

Grevel, K.D., and Majzlan, J. (2009) Internally consistent thermodynamic data for magnesium sulfate hydrates. Geochimica et Cosmochimica Acta, 73, 6805–6815.

——— (2011) Internally consistent thermodynamic data for metal divalent sulphate hydrates. Chemical Geology, 286, 301–306.

Grotzinger, J.P., Sumner, D.Y., Kah, L.C., Stack, K., Gupta, S., Edgar, L., Rubin, D., Lewis, K., Schieber, J., Mangold, N., and others. (2014) A habitable fluvio-lacustrine environment at Yellowknife Bay, Gale Crater, Mars. Science, 343, doi:10.1126/science.1242777.

Grotzinger, J.P., Gupta, S., Malin, M.C., Rubin, D.M., Schieber, J., Siebach, K., Sumner, D.Y., Stack, K.M., Vasavada, A.R., Arvidson, R.E., and others. (2015) Deposition, exhumation, and paleoclimate of an ancient lake deposit, Gale crater, Mars. Science, 350, doi:10.1126/science.aac7575.

Gruninger, J.H., Ratkowski, A J., and Hoke, M.L. (2004) The sequential maximum angle convex cone (SMACC) endmember model. In S.S. Shen and P.E. Lewis, Eds., Proceedings SPIE, Algorithms and Technologies for Multispectral, Hyperspectral, and Ultraspectral Imagery X, 5425, doi:10.1117/12.543794.

Herkenhoff, K.E., Squyres, S.W., Bell, J.F., Maki, J.N., Arneson, H.M., Bertelsen, P., Brown, D.I., Collins, S.A., Dingizian, A., Elliott, S.T., and others. (2003) Athena Microscopic Imager investigation. Journal of Geophysical Research: Planets, 108, 8065, doi:10.1029/2003JE002076.

Herkenhoff, K.E., Squyres, S.W., Anderson, R., Archinal, B.A., Arvidson, R.E., Barrett, J.M., Becker, K.J., Bell, J.F. III, Budney, C., Cabrol, N.A., and others. (2006), Overview of the Microscopic Imager Investigation during Spirit's first 450 sols in Gusev crater. Journal of Geophysical Research: Planets, 111, E02S04.

Hinkle, M.A.G. (2015) Ion interactions at the mineral-water interface during biogeochemical iron and manganese cycling, Ph.D. thesis, Washington University, St. Louis, doi:10.7936/K7JQ0Z58.

Kelly, K.L., and Judd, D.B. (1976) Color: Universal Language and Dictionary of Names, 196 p. U.S. Department of Commerce, National Bureau of Standards.

Kenkmann, T., Poelchau, M.H., and Wulf, G. (2014) Structural geology of impact craters. Journal of Structural Geology, 62, 156–182.

Klein, C. (2002) The 22nd Edition of the Manual of Mineral Science, 641 pp. Wiley, New York.

Kobylin, P.M., Sippola, H., and Taskinen, P.A. (2011) Thermodynamic modelling of aqueous Fe(II) sulfate solutions. CALPHAD, 35, 499–511.

Lanza, N. et al. (2015) Understanding the signature of rock coatings in laser-induced breakdown spectroscopy data. Icarus, 249, 62–73, doi:10.1016/j.icarus.2014.05.038.

Liu, T., and Broecker, W.S. (2008) Rock varnish evidence for latest Pleistocene millennial-scale wet events in the drylands of Western United States. Geology, 36, 403–406, doi:10.1130/G24573A.1.

Majzlan, J., Navrotsky, A., and Schwertmann, U. (2004a) Thermodynamics of iron oxides: Part III. Enthalpies of formation and stability of ferrihydrite (~$Fe(OH)_3$), schwertmannite (~$FeO(OH)_{3/4}(SO_4)_{1/8}$), and ε-$Fe_2O_3$. Geochimica et Cosmochimica Acta, 68, 1049–1059.

Majzlan, J., Stevens, R., Boerio-Goates, J., Woodfield, B.F., Navrotsky, A., Burns, P.C., Crawford, M.K., and Amos, T.G. (2004b) Thermodynamic properties, low-temperature heat-capacity anomalies, and single-crystal X-ray refinement of hydronium jarosite, $(H_3O)Fe_3(SO_4)_2(OH)_6$. Physics and Chemistry of Minerals, 31(8), 518–531.

Marion, G.M., Catling, D.C., and Kargel, J.S. (2003) Modeling aqueous ferrous iron chemistry at low temperatures with application to Mars. Geochimica et Cosmochimica Acta, 67(22), 4251–4266.

Marion, G.M., Kargel, J.S., and Catling, D.C. (2008) Modeling ferrous-ferric iron chemistry with application to Martian surface geochemistry. Geochimica et

Cosmochimica Acta, 72(1), 242–266.
Marion, G.M., Crowley, J.K., Thomson, B.J., Kargel, J.S., Bridges, N.T., Hook, S.J., Baldridge, A., Brown, A.J., da Luz, B.R., and de Souza, C.R. (2009) Modeling aluminum-silicon chemistries and application to Australian acidic playa lakes as analogues for Mars. Geochimica et Cosmochimica Acta, 73(11), 3493–3511.
Marion, G.M., Catling, D.C., Zahnle, K.J., and Claire, M.W. (2010) Modeling aqueous perchlorate chemistries with applications to Mars. Icarus, 207(2), 675–685.
McEwen, A.S., Eliason, E.M., Bergstrom, J.W., Bridges, N.T., Hansen, C.J., Delamere, W.A., Grant, J.A., Gulick, V.C., Herkenhoff, K.E., Keszthelyi, L., and others. (2007) Mars Reconnaissance Orbiter's High Resolution Imaging Science Experiment (HiRISE). Journal of Geophysical Research: Planets, 112, E05S02, doi:10.1029/2005JE002605.
Milton, D.J., Barlow, B.C., Brett, R., Brown, A.R., Glikson, A.Y., Manwaring, E.A., Moss, F.J., Sedmik, E.C.E., Van Son, J., and Young, G.A. (1972) Gosses Bluff impact structure, Australia. Science, 175, 1199–1207.
Morris, R.V., Golden, D.C., Bell, J.F. III, Lauer, H.V. Jr., and Adams, J.B. (1993) Pigmenting agents in Martian soils: Inferences from spectral, Mössbauer, and magnetic properties of nanophase and other iron oxides in Hawaiian palagonitic soil PN-9. Geochimica et Cosmochimica Acta, 57, 4597–4609.
Morris, R.V., Klingelhöfer, G., Schröder, C., Rodionov, D.S., Yen, A., Ming, D.W., de Souza, P.A., Wdowiak, T., Fleischer, I., Gellert, R., and others. (2006) Mössbauer mineralogy of rock, soil, and dust at Meridiani Planum, Mars: Opportunity's journey across sulfate-rich outcrop, basaltic sand and dust, and hematite lag deposits. Journal of Geophysical Research: Planets, 111, E12S15.
Osinski, G.R., and Pierazzo, E. (2012) Impact Cratering: Processes and Products, 330 p. Wiley-Blackwell, Hoboken, New Jersey.
Osinski, G.R., and Spray, J.G. (2005) Tectonics of complex crater formation as revealed by the Haughton impact structure, Devon Island, Canadian High Arctic. Meteoritics and Planetary Science, 40, 1813–1834.
Post, J.E. (1999) Manganese oxide minerals: Crystal structures and economic and environmental significance. Proceedings of the National Academy of Sciences, 96, 3447–3454, doi:10.1073/pnas.96.7.3447.
Poulet, F., Bibring, J.-P., Mustard, J.F., Gendrin, A., Mangold, N., Langevin, Y., Arvidson, R.E., Gondet, B., Gomez, C., Berthé, M., and others. (2005) Phyllosilicates on Mars and implications for early Martian climate. Nature, 438, 623–627, doi:10.1038/nature04274.
Rice, M.S., Bell, J.F. III, Cloutis, E.A., Wang, A., Ruff, S.W., Craig, M.A., Bailey, D. T., Johnson, J.R., de Souza Jr., P.A., and Farrand, W.H. (2010) Silica-rich deposits and hydrated minerals at Gusev Crater, Mars: Vis-NIR spectral characterization and regional mapping. Icarus, 205, 375–395.
Sherman, D.M. (1984) The electronic structures of manganese oxide minerals. American Mineralogist, 69, 788–799.
Squyres, S.W., Arvidson, R.E., Baumgartner, E.T., Bell, J.F., Christensen, P.R., Gorevan, S., Herkenhoff, K.E., Klingelhöfer, G., Madsen, M.B., Morris, R.V., and others. (2003) Athena Mars rover science investigation. Journal of Geophysical Research: Planets, 108, 8062, doi:10.1029/2003JE002121.
Squyres, S.W., Arvidson, R.E., Bell, J.F., Calef, F., Clark, B.C., Cohen, B.A., Crumpler, L.A., Souza, P.A. de, Farrand, W.H., Gellert, R., and others. (2012) Ancient impact and aqueous processes at Endeavour crater, Mars. Science, 336, 570–576, doi:10.1126/science.1220476.
Stöffler, D., Artemieva, N.A., Wunnemann, K., Reimold, W.U., Jacob, J., Hansen, B.K., and Summerson, I.A.T. (2013) Ries crater and suevite revisited-observations and modeling, Part I: observations. Meteoritics & Planetary Science, 48, 515–589, doi:10.1111/maps.12086.
Tosca, N.J., McLennan, S.M., Clark, B.C., Grotzinger, J.P., Hurowitz, J.A., Knoll, A.H., Schroder, C., and Squyres, S.W. (2005) Geochemical modeling of evaporation processes on Mars: Insight from the sedimentary record at Meridiani Planum. Earth and Planetary Science Letters, 240, 122–148.
Tosca, N.J., Smirnov, A., and McLennan, S.M. (2007) Application of the Pitzer ion interaction model to isopiestic data for the $Fe_2(SO_4)_3$-H_2SO_4-H_2O system at 298.15 and 323.15 K. Geochimica et Cosmochimica Acta, 71, 2680–2698.
Van Bommel, S.J., Gellert, R., Berger, J.A., Campbell, J.L., Thompson, L.M., Edgett, K.S., McBride, M.J., Minitti, M.E., Pradler, I., and Boyd, N.I. (2016) Deconvolution of distinct lithology chemistry through oversampling with the Mars Science Laboratory Alpha Particle X-ray Spectrometer. Journal of X-ray Spectrometry, 45, 155–161, doi:10.1002/xrs.2681.
Vaughan, D.J., and Rosso, K.M. (2006) Chemical bonding in sulfide minerals. Reviews in Mineralogy and Geochemistry, 61, 231–264.
Wolters, F., Lagaly, G., Nueeshsch, R., and Emmerich, K. (2009) A comprehensive characterization of dioctahedral smectites. Clays and Clay Minerals, 57, 115–133, doi:10.1346/CCMN. 2009.0570111.

Manuscript received October 20, 2015
Manuscript accepted February 5, 2016
Manuscript handled by Richard April